JGP Journal of General Physiology

HYPOTHESIS

Excitation–Contraction Coupling

Modeling the mechanism of Ca^{2+} release in skeletal muscle by DHPRs easing inhibition at RyR I1-sites

D. George Stephenson[1]

Ca^{2+} release from the sarcoplasmic reticulum (SR) plays a central role in excitation–contraction coupling (ECC) in skeletal muscles. However, the mechanism by which activation of the voltage-sensors/dihydropyridine receptors (DHPRs) in the membrane of the transverse tubular system leads to activation of the Ca^{2+}-release channels/ryanodine receptors (RyRs) in the SR is not fully understood. Recent observations showing that a very small Ca^{2+} leak through RyR1s in mammalian skeletal muscle can markedly raise the background [Ca^{2+}] in the junctional space (JS) above the Ca^{2+} level in the bulk of the cytosol indicate that there is a diffusional barrier between the JS and the cytosol at large. Here, I use a mathematical model to explore the hypothesis that a sudden rise in Ca^{2+} leak through DHPR-coupled RyR1s, caused by reduced inhibition at the RyR1 Ca^{2+}/Mg^{2+} inhibitory I1-sites when the associated DHPRs are activated, is sufficient to enable synchronized responses that trigger a regenerative rise of Ca^{2+} release that remains under voltage control. In this way, the characteristic response to Ca^{2+} of RyR channels is key not only for the Ca^{2+} release mechanism in cardiac muscle and other tissues, but also for the DHPR-dependent Ca^{2+} release in skeletal muscle.

Introduction

The activity of the skeletal muscle of vertebrates is regulated in the main by voltage sensors/dihydropyridine receptors (DHPRs) in the membrane of the transverse (t-) tubular system (Schneider and Chandler, 1973; Ríos and Brum, 1987; Ríos and Pizarro, 1991; Melzer et al., 1995) and the intracellular [Mg^{2+}], which exerts a powerful inhibitory action on the ryanodine receptors (RyRs)/sarcoplasmic reticulum (SR) Ca^{2+}-release channels in terminal cisternae of the SR (Lamb and Stephenson, 1991, 1994; Lamb, 2002a, 2002b; Dulhunty, 2006; Stephenson, 2006). DHPRs physically interact with RyRs in the narrow junctional space (JS) between t-system and SR membranes at triads, where t-tubules are flanked in close apposition by two terminal cisternae of the SR. The size of the gap at triads between t-tubule and SR membranes is critical for enabling functional crosstalk between DHPRs and RyRs and is primarily determined by junctophilin-1 proteins, JPH-1s, that directly interact at their tubular membrane end (N-terminal region) with DHPRs and at their SR membrane end (C-terminal region) with the respective DHPR-coupled RyR1 (Landstrom et al., 2014; Perni, 2022; Lehnart and Wehrens, 2022). The RyRs in the JS are organized in checkered arrays (Block et al., 1988; Franzini-Armstrong and Nunzi, 1983; Franzini-Armstrong et al., 1998) with every second RyR being physically coupled to a group of four DHPRs forming a tetrad, such that each DHPR in the tetrad is in physical contact with one of the four subunits (protomers) of a RyR. There is broad agreement about a direct line of communication that ensures fast signal transmission from DHPRs activated by t-system membrane depolarization to DHPR-coupled RyRs, but the exact nature of the molecular interactions between skeletal DHPRs and RyRs in the JS remains unclear.

All RyRs immediately adjacent to each other, together with the associated proteins form a couplon (Stern et al., 1997; Franzini-Armstrong et al., 1999), such that triads effectively have two couplons, one on each side of the t-tubule that function independently of each other. In addition to couplons localized in the JS of all vertebrates, non-mammalian skeletal muscles also have variable groups of RyRs on the SR terminal cisternae located outside the JS in parajunctional arrays that do not face t-tubules and do not have contact with DHPRs or RyRs in couplons (Felder and Franzini-Armstrong, 2002).

Skeletal muscles of adult mammals contain almost exclusively the RyR1 isoform, which is one of the three RyR isoforms

[1]Department of Microbiology, Anatomy, Physiology and Pharmacology, La Trobe University, Melbourne, Australia.

Correspondence to D. George Stephenson: george.stephenson@latrobe.edu.au

This work is part of a special issue on excitation–contraction coupling.

(RyR1–3) expressed in mammalian tissues. In contrast, skeletal muscles from non-mammalian vertebrates, like frogs—which served for many years as the animal model of choice for investigating the mechanism of excitation–contraction coupling (ECC) in skeletal muscle—express in similar amounts two RyR isoforms: α-RyR and β-RyR, which are homologs of the mammalian isoforms RyR1 and RyR3, respectively (Sutko and Airey, 1996; Murayama et al., 2000; Lanner et al., 2010; Murayama and Kurebayashi, 2011).

There is strong evidence that all couplons in skeletal muscles of mammals and non-mammalian vertebrates consist of RyR1s/α-RyRs and that the parajunctional groups of RyRs found predominantly in non-mammalian muscles consist of RyR3s/β-RyRs (Felder and Franzini-Armstrong, 2002; Perni et al., 2015). The abundant parajunctional arrays of β-RyRs in non-mammalian vertebrate skeletal muscle appear to support and possibly amplify the DHPR-activation-induced Ca^{2+} release that occurs at the level of couplons, considering, for example, that there are two triads (i.e., four RyR1 couplons) per sarcomere in mammalian skeletal muscle, but only one triad (i.e., two α-RyRs couplons and several β-RyRs parajunctional arrays) per sarcomere of similar length in frog skeletal muscle.

The relative ease of purification of the RyR1 isoform from skeletal muscles of mammals together with its relevance to human conditions contributed to the fact that the RyR1 isoform is the most extensively studied RyR isoform and its ionic control mechanisms are best understood. Manifestly, skeletal muscle fibers of mammals are uniquely suited for investigating how voltage-dependent DHPR activation interacts with ionic control mechanisms of RyR1 activation.

Cully et al. (2018) (see also Barclay and Launikonis, 2022) have shown that the average $[Ca^{2+}]$ in the JS ($[Ca^{2+}]_{js}$) of human skeletal muscle fibers at rest is considerably greater than that in the bulk of the cytosol ($[Ca^{2+}]_c$) and that $[Ca^{2+}]_{js}$ approaches $[Ca^{2+}]_c$ only when the RyR1s are fully blocked. Similarly, Despa et al. (2014) showed a standing diastolic $[Ca^{2+}]$ difference in cardiac myocytes between the cleft (which is equivalent to the JS in skeletal muscle fibers) and the cytosol at large, produced primarily by the diastolic SR Ca^{2+} leak through the cardiac RyR2s. Furthermore, Sanchez et al. (2021) used a Ca^{2+}-sensitive fluorescent probe targeted to the JS in mouse skeletal muscle fibers and obtained results that are consistent with $[Ca^{2+}]_{js}$, being several times greater than $[Ca^{2+}]_c$ at rest. These observations suggest that a diffusional barrier exists between the JS and most of the cytosol (JS/cytosol barrier), causing JS to function as an intermediate compartment between the SR cisternae and the cytosol at large.

JS, as part of the cytosol, plays a central role in the regulation of SR Ca^{2+} release because all cytoplasmic regulatory sites on the RyR1s/α-RyRs in a couplon are exposed to the JS rather than to the bulk of the cytosol. For each of the four protomers of one RyR1, there is a Ca^{2+} activation site (Ca^{2+} A-site), an ATP-binding site, a caffeine-binding site, and a low-affinity Ca^{2+}/Mg^{2+} inhibitory I1 site. The location of the Ca^{2+} A-sites, the ATP sites, and the caffeine-binding sites on the cytoplasmic shell of the RyR1 has been specifically determined in cryo-EM reconstructions by Des Georges et al. (2016). These sites are located close to each other and are part of a "control hub" that regulates the opening of the RyR1 gate (Des Georges et al., 2016). After ATP is bound to its specific sites on the RyR1s in muscle, the control hub is primed to open the RyR1 gate when Ca^{2+} binds to the A-sites and the inhibitory low-affinity Ca^{2+}/Mg^{2+} I1-sites are unoccupied (Nayak and Samsó, 2022). The low-affinity Ca^{2+}/Mg^{2+} I1-sites are situated in the four E-F domains located outside the control hub, at the base of the huge mushroom-like cytosolic shell of the RyR1 (Laver et al., 1997a; Nayak et al., 2024), which rotates outward and downward toward its basis when the control hub is activated to open the RyR1 pore (Des Georges et al., 2016).

Employing a mathematical model based on the role of ionic control mechanisms of RyR1 function developed in the Appendix, I explore here the hypothesis that a sudden rise in Ca^{2+} leak in the JS through DHPR-coupled RyR1s in couplons, caused by reduction of inhibition at the RyR1 Ca^{2+}/Mg^{2+} inhibitory I1-sites when the associated DHPRs are activated, is sufficient to enable synchronized responses that trigger a regenerative rise of Ca^{2+} release that remains under voltage control.

Materials and methods

Data S1, S2, S3, S4, S5, and S6 consist of simulations of SR Ca^{2+} release in skeletal muscle using the mathematical model described in the article under the various conditions mentioned in the text, performed with Wolfram Mathematica online. The program scripts and simulation outputs refer to model predictions for Ca^{2+} release upon stimulation (1) under physiological conditions when the SR is either normally loaded, or severely depleted of Ca^{2+}, without SR Ca^{2+} uptake (Data S1), (2) under physiological conditions with strong SR Ca^{2+} uptake (Data S2), (3) in the presence of 10 mM BAPTA when the SR is either normally loaded, or severely depleted of Ca^{2+} (Data S3), (4) in the presence of 10 mM EGTA when the SR is either normally loaded or severely depleted of Ca^{2+} (Data S4), (5) under physiological conditions at submaximal levels of DHPR-activation (Data S5), and (6) in the presence of 20 mM BAPTA at increased ionic strength with SR severely depleted of Ca^{2+} (Data S6).

Online supplemental material

Data S1, S2, S3, S4, S5, and S6 provide Wolfram Mathematica online program scripts.

Development and validation of the mathematical model

JS holds the key to understanding how the mechanism of SR Ca^{2+} release works

In principle, the time-dependent changes in $[Ca^{2+}]_{js}$ ($[Ca^{2+}]_{js}(t)$) are determined by differential Eq. 1, where Ca^{2+}– *inflow (t)* refers to the rate of Ca^{2+} entry into the JS and Ca^{2+}– *outflow (t)* refers to the rate of Ca^{2+} exit from the JS:

$$d[Ca^{2+}]_{js}(t)/dt = Ca^{2+} - inflow(t) - Ca^{2+} - outflow(t) \quad (1)$$

In the presence of a steady Ca^{2+} inflow into the JS from the SR through the RyR1s/α-RyRs, as would be the case in a muscle fiber at rest, a steady state is reached such that the Ca^{2+} outflow

from the JS into the cytosol at large balances the Ca^{2+} inflow. Considering that most Ca^{2+} entry into the JS is through junctional RyR1s/α-RyRs, Ca^{2+} inflow into the JS can be quantified as the product between a parameter k_{SRJS} that describes SR membrane permeability (measured in ms^{-1}) and the $[Ca^{2+}]$ difference across the SR junctional membrane between $[Ca^{2+}]$ in the SR cisternae, $[Ca^{2+}]_{SR}$, and $[Ca^{2+}]_{js}$. Similarly, Ca^{2+} outflow from the JS is quantified as the product between k_{diff} that describes the diffusiveness of Ca^{2+} across JS/cytosol barrier (also measured in ms^{-1}) and the difference between $[Ca^{2+}]_{js}$ and bulk cytosolic $[Ca^{2+}]$, $[Ca^{2+}]_c$. Therefore, at rest,

$$k_{SRJS}\left([Ca^{2+}]_{SR} - [Ca^{2+}]_{js}\right) = k_{diff}\left([Ca^{2+}]_{js} - [Ca^{2+}]_c\right), \quad (2)$$

and

$$[Ca^{2+}]_{js} = \left(k_{SRJS}[Ca^{2+}]_{SR} + k_{diff}[Ca^{2+}]_c\right)/\left(k_{SRJS} + k_{diff}\right) \quad (3)$$

Importantly, k_{SRJS} can be determined at a steady state using Eq. 4, when k_{diff}, $[Ca^{2+}]_{js}$, $[Ca^{2+}]_{SR}$, and $[Ca^{2+}]_c$ values are known:

$$k_{SRJS} = k_{diff}\left([Ca^{2+}]_{js} - [Ca^{2+}]_c\right)/\left([Ca^{2+}]_{SR} - [Ca^{2+}]_{js}\right) \quad (4)$$

Furthermore, considering that the ratio of DHPR-coupled to DHPR-noncoupled RyR1s/α-RyRs in a couplon is 1:1, it follows that k_{SRJS} changes in proportion to the number n of RyR1s/α-RyRs in a couplon and the mean value between the open probability of one DHPR-coupled ($^{c}P_O$) and one DHPR-noncoupled RyR1/α-RyR ($^{nc}P_O$):

$$k_{SRJS} = \gamma n(^{c}P_O + {}^{nc}P_O)/2 = 0.5\gamma n(^{c}P_O + {}^{nc}P_O), \quad (5)$$

where γ is a constant with the dimension of ms^{-1}.

Since the cytosolic regulatory sites on RyR1s/α-RyRs in situ are exposed to the JS rather than to the cytosol at large, it follows that the open probability of both DHPR-noncoupled and DHPR-coupled RyRs are sensitive to the ionic concentrations in the JS environment. Eqs. 6 and 7 describe the dependency of the open probability of DHPR-noncoupled RyR1s, $^{nc}RyR1s$, ($^{nc}P_O$), and DHPR-coupled RyR1s, $^{c}RyR1s$ ($^{c}P_O$), respectively, on $[Ca^{2+}]_{js}$, $[Mg^{2}]_{js}$, total $[Ca^{2+} + Mg^{2+}]_{js} = [CaMg]_{js}$, monovalent metallic cation concentration ($[M_m^{+}]_{js}$), and SR luminal Ca^{2+} ($[Ca^{2+}]_{SR}$). The equations are derived for steady-state conditions in Appendix 1 as Eqs. A14 and A15 within the framework of the dual-inhibition model by Mg^{2+} of RyR1 activity at the Ca^{2+} A-sites and low-affinity inhibitory Ca^{2+}/Mg^{2+} I1 sites in the presence of millimolar ATP, considering structural features of the RyR1 molecules. As described in Appendix 1, Eq. 6/Eq. A14 quantitatively explains the RyR1 open probability measurements made on isolated RyR1s incorporated in lipid bilayers (Laver et al., 1997b; Laver, 2018) and Ca^{2+} fluxes from Ca^{2+}-loaded heavy SR vesicles (Meissner, 1984, 1986), while Eq. 7/Eq. A15 considers evidence that DHPRs can exert an additional inhibitory action on (DHPR-coupled) RyR1s in skeletal muscle fibers at rest (see Kirsch et al., 2001; Zhou et al., 2006; and references therein).

The first term in Eqs. 6 and 7, P_{AO}, describes the probability of activation at the Ca^{2+} A-sites of either $^{nc}RyR1s$ or $^{c}RyR1s$ when the four protomeric A-sites of the RyR1s are activated. The values of the protomeric parameters $^{1p}P_i$, $^{1p}P_{max}$, $^{1p}K_{Mm}{}^{2}$, $^{1p}K_{CaA}$, $^{1p}K_{Mg}$, and $^{1p}K_L$ are shown in Table 1 and were derived from experimental observations as described in Appendix 1. $^{1p}P_i$ characterizes the probability of an individual A-site activation in the absence of Ca^{2+} and Mg^{2+} in the JS (or cytosol) when the A-site is free or has two M_m^{+} bound to it, while $^{1p}P_{max}$ describes the probability of an individual Ca^{2+} A-site activation when the A-site is occupied by Ca^{2+}. $^{1p}K_{Mm}{}^{2}$ is the dissociation constant of two M_m^{+} from the Ca^{2+} A-site, considering that a divalent cationic site is likely to bind two M_m^{+}, $^{1p}K_{CaA}$ is the Ca^{2+} dissociation constant from the Ca^{2+} A-site and $^{1p}K_{Mg}$ is the Mg^{2+} dissociation constant from the Ca^{2+} A-site when the SR is depleted of Ca^{2+} ($[Ca^{2+}]_{SR} = 0$), and $^{1p}K_L$ is the Ca^{2+} dissociation constant from the luminal SR Ca^{2+} site, whose occupancy by Ca^{2+} alters the Mg^{2+} dissociation constant of the corresponding A-site as discussed in Appendix 1.

The second terms, $^{nc}P_{IO}$, in Eq. 6 and $^{c}P_{IO}$ in Eq. 7, describe the probabilities that the pores of $^{nc}RyR1s$ or $^{c}RyR1s$ channels are not blocked from opening by inhibition at their respective Ca^{2+}/Mg^{2+} I1-sites. As explained in the Appendix, the Hill Equation with a Hill coefficient of 2 that was used to fit experimental results on Ca^{2+}/Mg^{2+} inhibition at the I1-sites of isolated RyR1s incorporated in lipid bilayers was deemed to also describe inhibition at the $^{nc}RyR1s$ in muscle. In contrast, the enhanced inhibitory action exerted by DHPRs on $^{c}RyR1s$ was considered to result from an increased level of cooperativity between the four protomers in the $^{c}RyR1$ that produces quasi-simultaneous binding and dissociation of four Ca^{2+}/Mg^{2+} ions by a two-state allosteric mechanism (see e.g., Viappiani et al., 2014) at the Ca^{2+}/Mg^{2+} inhibitory I1-sites, such that $^{c}RyR1$ channels are blocked from opening at the Ca^{2+}/Mg^{2+} inhibitory I1-sites when all four I1-inhibitory sites are occupied, and the channels are allowed to open when all four I1-inhibitory sites are free.

The apparent affinity of the I1 sites for Ca^{2+} and Mg^{2+} is particularly sensitive to the ionic strength concentration, which is not the case for the Ca^{2+} A-sites (Shomer et al., 1993; Meissner et al., 1997; Laver et al., 2004). For the ionic conditions prevalent in mammalian skeletal muscle, it is broadly agreed that 50% inhibition at the low-affinity Ca^{2+}/Mg^{2+} I1-sites of RyR1s occurs at $[Ca^{2+}]_c + [Mg^{2+}]_c$ ($[CaMg]_c$) in the range of 50 µM (Donoso et al., 2000) to 100 µM (Meissner, 1984, 1986; Laver et al., 1997b; Laver, 2018). In calculations, it was assumed that 50% inhibition at the low-affinity Ca^{2+}/Mg^{2+} I1-sites of $^{c}RyR1s$ and $^{nc}RyR1s$ at rest occurs at ≈50 µM Mg^{2+} (and Ca^{2+}) because the results of Donoso et al. (2000) were obtained on native triads of fast-twitch rabbit muscle, where the arrangement of RyR1s and DHPRs in the JS is closest to that in the living muscle at rest. Accordingly, both K_{in} for $^{nc}RyR1s$ and $^{4p}K_{in}$ for $^{c}RyR1s$ in Table 1 equal 0.05 mM.

$$^{nc}P_O = P_{AO} \times {}^{nc}P_{IO} = \frac{\left({}^{1p}P_i\left(1 + \frac{[M_m]_{js}^2}{({}^{1p}K_{Mm})^2}\right) + {}^{1p}P_{max}\frac{[Ca^{2+}]_{js}}{{}^{1p}K_{CaA}}\right)^4}{\left(1 + \frac{[M_m]_{js}^2}{({}^{1p}K_{Mm})^2} + \frac{[Ca^{2+}]_{js}}{{}^{1p}K_{CaA}} + \frac{[Mg^{2+}]_{js}}{{}^{1p}K_{Mg}\left(1+\frac{[Ca^{2+}]_{SR}}{{}^{1p}K_L}\right)}\right)^4} \times \frac{1}{1 + \left(\frac{[CaMg]_{js}}{K_{in}}\right)^2} \quad (6)$$

Table 1. **Parameter values used to quantitatively describe the activation of DHPR-coupled RyR1s, ^{c}*RyR1s*, ($^{c}P_O$), and DHPR-noncoupled RyR1s, ^{nc}*RyR1s* ($^{nc}P_O$) *under different conditions***

Parameter	Description	Parameter value
$^{1p}K_{Mm}$	Apparent dissociation constant of Mm^+ from individual A-sites of ^{c}*RyR1s* and ^{nc}*RyR1s*	172.1 mM[a]
$^{1p}K_L$	Ca^{2+} equilibrium dissociation constant from individual SR luminal sites of ^{c}*RyR1s* and ^{nc}*RyR1s*	346.6 μM[a]
$^{1p}K_{Mg}$	Mg^{2+} equilibrium dissociation constant from individual A-sites of ^{c}*RyR1s* and ^{nc}*RyR1s*	30.65 μM[a]
$^{1p}K_{CaA}$	Ca^{2+} equilibrium dissociation constant from individual A-sites of ^{c}*RyR1s* and ^{nc}*RyR1s*	70 nM[a]
$^{1p}P_{max}$	Level of individual A-site activation in ^{c}*RyR1s* and ^{nc}*RyR1s* when the A-site is occupied by Ca^{2+}	0.963[a]
$^{1p}P_i$	Level of individual A-site activation in ^{c}*RyR1s* and ^{nc}*RyR1s* when the A-site is free or is occupied by two Mm^+; $^{1p}P_i$ is sensitive to SR luminal Ca^{2+} ($[Ca^{2+}]_L$)	= 0.56 + 0.35/(1 + 0.25 mM/$[Ca^{2+}]_L$)[a]
K_{in}	Apparent Ca^{2+}/Mg^{2+} dissociation constant from I1 sites of ^{nc}*RyR1s*	0.05 mM[b]
$^{4p}K_{in}$	Apparent Ca^{2+}/Mg^{2+} dissociation constant from I1 sites of ^{c}*RyR1s* when DHPRs are not activated	0.05 mM[b]
$^{4p}K_{in}$	Apparent Ca^{2+}/Mg^{2} dissociation constant from I1 sites of ^{c}*RyR1s* when the DHPRs are activated	1.5 mM[c]

[a]Parameter value derived in Appendix 1 from experimental data of Laver et al. (2004).
[b]Parameter value derived from experimental data of Donoso et al. (2000).
[c]As described in the text, DHPR activation of ^{c}*RyR1s* induces a sudden 30-fold rise of $^{4p}K_{in}$ from its resting level in ^{c}*RyR1s*, which eases inhibition at the I1-sites of the respective ^{c}*RyR1s*.

$$ {}^{c}P_O = P_{A0} \times {}^{c}P_{I0} = \frac{\left({}^{1p}P_i\left(1+\frac{[M_m]_{js}^2}{({}^{1p}K_{Mm})^2}\right)+{}^{1p}P_{max}\frac{[Ca^{2+}]_{js}}{{}^{1p}K_{CaA}}\right)^4}{\left(1+\frac{[M_m]_{js}^2}{({}^{1p}K_{Mm})^2}+\frac{[Ca^{2+}]_{js}}{{}^{1p}K_{CaA}}+\frac{[Mg^{2+}]_{js}}{{}^{1p}K_{Mg}\left(1+\frac{[Ca^{2+}]_{SR}}{{}^{1p}K_L}\right)}\right)^4} \times \frac{1}{1+\frac{\left([CaMg]_{js}\right)^4}{\left({}^{4p}K_{in}\right)^4}} \quad (7) $$

Barclay and Launikonis (2022) estimated the Ca^{2+} inflow into the JS from the SR through the *RyR1s* (k_{SRJS} ($[Ca^{2+}]_{SR}$–$[Ca^{2+}]_{js}$) at 3.8 μM ms^{-1} in skeletal human muscle fibers at rest when $[Ca^{2+}]_{SR}$ = 400 μM (Ziman et al., 2010) and $[Ca^{2+}]_c$ was buffered at 67 nM with 50 mM EGTA, which has its main molecular forms: H_2EGTA^{2-} and Ca-$EGTA^{2-}$ negatively charged. Under these conditions, k_{diff}, which characterizes the diffusiveness of Ca^{2+} across the JS/cytosol barrier, was evaluated at 28 ms^{-1}. Using these values in Eq. 2, $[Ca^{2+}]_{js}$ = 203 nM (3.8 μM ms^{-1}/28 ms^{-1} + 67 nM), and from Eq. 4, k_{SRJS} = 9.525 s^{-1} (28,000 s^{-1} × 0.136 μM/399.8 μM) at rest.

Note that the ability of a steady Ca^{2+} leak Lk = 3.8 μM ms^{-1} into the JS to generate a difference between $[Ca^{2+}]_{js}$ and $[Ca^{2+}]_c$ in the order of 10–130 nM in the presence of 50 mM total EGTA ($[EGTA]_T$) when $[Ca^{2+}]_c$ = 67 nM (Cully et al., 2018; Barclay and Launikonis, 2022) is only possible if the diffusiveness of H_2EGTA^{2-} and Ca-$EGTA^{2-}$ across the JS/cytosol barrier ($k_{diffEGTA}$) is several orders of magnitude lower than that for Ca^{2+} (k_{diff} = 28 ms^{-1}). This is because the difference between $[Ca^{2+}]_{js}$ and $[Ca^{2+}]_c$ generated by a steady Ca^{2+} leak into the JS is given by the ratio $\frac{Lk}{k_{diff}+k_{diffEGTA}\frac{K_D[EGTA]_T}{(K_D+[Ca^{2+}]_{js})(K_D+[Ca^{2+}]_c)}}$, where K_D is the equilibrium dissociation constant of Ca^{2+} from CaEGTA^{2-} (~185 nM). Accordingly, a Ca^{2+} leak of 3.8 μM ms^{-1} when $[Ca^{2+}]_c$ = 67 nM would generate a $[Ca^{2+}]_{js}$–$[Ca^{2+}]_c$ difference of 10 or 130 nM when $k_{diffEGTA}$ = 2.5 s^{-1} (= 8.97 × 10^{-5} k_{diff}) or 0.0127 s^{-1} (= 4.56 × 10^{-7} k_{diff}), respectively. Notice that a diffusiveness of H_2EGTA^{2-} and Ca-$EGTA^{2-}$ across the barrier in the order of 0.0127 s^{-1} necessitates several minutes for $[EGTA]_T$ to equilibrate between JS and the rest of the cytosol and indicates that little H_2EGTA^{2-} and Ca-$EGTA^{2-}$ is exchanged across the barrier over <100 ms. In principle, a situation where the diffusiveness of H_2EGTA^{2-} and Ca-$EGTA^{2-}$ can be orders of magnitude smaller than that for Ca^{2+} would occur if the JS/cytosol barrier in muscle fibers at rest was negatively charged with relatively small pores.

The estimated values of $^{nc}P_O$ and $^{c}P_O$ for resting conditions ($[Ca^{2+}]_{js}$ = 203 nM, $[Ca^{2+}]_{SR}$ = 400 μM, $[Mg^{2+}]_{js}$ = 1 mM, $[M_{m^+}]_{js}$ = 150 mM, and parameter values in Table 1) are 4.84 × 10^{-6} and 1.21 × 10^{-8} using Eqs. 6 and 7, respectively, indicating that ^{nc}*RyR1s* are the main contributors to the RyR1s Ca^{2+} leak at rest. One can now calculate from Eq. 5 that γ = 3,927.8 n^{-1} ms^{-1} [9.525 s^{-1}/(0.5 n × 4.85 × 10^{-6})] in a couplon containing n RyR1s. (Note that the typical number of RyRs per couplon is about 40 in both mammalian and non-mammalian vertebrate skeletal muscle [Franzini-Armstrong et al., 1999]). The dependence of k_{SRJS} on ($^{c}P_O$ + $^{nc}P_O$) is then obtained by substituting γ back in Eq. 5:

$$ k_{SRJS} = 1,964({}^{c}P_O + {}^{nc}P_O)ms^{-1}. \quad (8) $$

Regarding the magnitude of k_{diff}, the value of 28 ms^{-1} estimated by Barclay and Launikonis (2022) in human skeletal muscle fibers under resting conditions can only support a maximum rate of Ca^{2+} release from the JS into the cytosol at large of 2.3 μM ms^{-1} (k_{diff} × maximum$[Ca^{2+}]_{js}$ × R, where R is the ratio between the JS volume and the volume of cytosolic water) since $[Ca^{2+}]_{js}$ cannot be greater than endogenous $[Ca^{2+}]_{SR}$ ≈ 400 μM and R ≈ 1/4,930 according to Table 3 in Barclay and Launikonis (2022). In comparison, the maximal SR Ca^{2+} release rate into the cytosol of mouse muscle fibers ranges between 55 and 200 μM ms^{-1} (see e.g., Sztretye et al., 2011; Baylor and Hollingworth, 2012), indicating

that k_{diff} needs to rise strongly above its resting level during stimulation to support much higher SR Ca^{2+} release rates.

Simple mechanisms for raising the value of k_{diff} following excitation can be envisaged like those used to open floodgates in a reservoir when the level of water in the reservoir exceeds a certain level. For example, a mechanism for raising the value of k_{diff} following excitation could involve the significant movement of the RyR1 cytosolic shells in the JS when the central control hubs are activated to open the RyR1 pores (Des Georges et al., 2016). Such movement can putatively alter the microarchitecture in the junctional gap between the SR and tubular membranes by altering interactions between JPHs, activated DHPRs, and RyRs with activated control hubs to increase the size of the junctional gap so as to allow Ca^{2+} to diffuse more freely from the JS into the rest of the cytosol. In the following calculations, it is assumed that k_{diff} rises linearly with the level of RyR1 activation at the Ca^{2+} A-sites, P_{A0}, from a base value of 14 ms^{-1} that is 50 % of the value (28 ms^{-1}) estimated by Barclay and Launikonis (2022) for resting conditions, i.e., k_{diff} = 14 ms^{-1} + b P_{A0}. In the presence of mM ATP, the value of P_{A0} also describes the activation level of RyR1 control hubs in a couplon that, in turn, determines the amount of movement in the RyR1 cytosolic shells that is associated with the magnitude of Ca^{2+} diffusiveness across the JS/cytosol barrier. Considering that k_{diff} = 28 ms^{-1} and P_{A0} = 0.00194 for resting conditions, it follows that $b \approx 7{,}216$ ms^{-1}, and therefore,

$$k_{diff} = (14 + 7,216 P_{A0})\,ms^{-1}. \quad (9)$$

Note that calsequestrin, which acts as a buffer for luminal Ca^{2+} in the SR cannot maintain $[Ca^{2+}]_{SR}$ close to its endogenous level of ~400 µM, when many RyR1s open simultaneously as shown by Sztretye et al. (2011). Considering a total endogenous SR Ca per SR volume of ~11 mM in fast-twitch mammalian muscle fibers (Fryer and Stephenson, 1996), it follows that about 10.6 mM Ca^{2+} is bound to calsequestrin at endogenous $[Ca^{2+}]_{SR}$ = 400 µM. Further, considering that calsequestrin has an apparent equilibrium Ca^{2+} dissociation constant of ~1 mM for $[Ca^{2+}]$ < 400 µM (Park et al., 2004), it implies that calsequestrin in the SR has a Ca^{2+} binding capacity, CSQ_{cap}, of ~37.1 mM per SR volume [= 10.6 mM (1 mM + 0.4 mM)/0.4 mM]. Since Ca^{2+} dissociates very fast from calsequestrin associated with junctional SR membranes (Beltrán et al., 2006) one can assume that Ca^{2+} bound to calsequestrin ($[CaCSQ(t)]$) in the SR is effectively in equilibrium with $[Ca^{2+}(t)]_{SR}$, such that at any time t, $[CaCSQ(t)]$ = 37.1 mM ($[Ca^{2+}(t)]_{SR}$/1 mM)/(1 + $[Ca^{2+}(t)]_{SR}$/1 mM). The time course of $[Ca^{2+}(t)]_{SR}$ in the presence of a rapid Ca^{2+} efflux from the SR is essentially given by the differential Eq. 10, where the SR–Ca^{2+}-release flux(t) expressed per SR volume is equivalent to the SR–Ca^{2+}-entry flux(t) into the JS volume reduced by the ratio between SR volume to JS volume (= 271 according to Table 3 in Barclay and Launikonis, 2022) and with changed sign:

$$d[Ca^{2+}(t)]_{SR}/dt = SR - Ca^{2+} - release\ flux(t) - d[CaCSQ(t)]/dt =$$
$$\frac{-1,964\ ms^{-1}\left([Ca^{2+}(t)]_{SR} - [Ca^{2+}(t)]_{js}\right)\left({}^{nc}P_0(t) + {}^{c}P_0(t)\right)}{271} - \frac{37.1}{\left(1 + \frac{[Ca^{2+}(t)]_{SR}}{1\ mM}\right)^2} d[Ca^{2+}(t)]_{SR}/dt,$$

or

$$d[Ca^{2+}(t)]_{SR}/dt = -7.25 ms^{-1}\left([Ca^{2+}(t)]_{SR} - [Ca^{2+}(t)]_{js}\right) \times \left({}^{nc}P_0(t) + {}^{c}P_0(t)\right) \times \frac{\left(1 + \frac{[Ca^{2+}(t)]_{SR}}{1mM}\right)^2}{37.1 + \left(1 + \frac{[Ca^{2+}(t)]_{SR}}{1mM}\right)^2}. \quad (10)$$

Proposed model for mechanism of DHPR-dependent activation of Ca^{2+} release in skeletal muscle

Experiments with mechanically skinned muscle fibers showed that the ability of DHPRs, when activated, to open RyR1s/α-RyRs in the presence of millimolar ATP, is facilitated when $[Mg^{2+}]_c$ is decreased below 1 mM, is curtailed when $[Mg^{2+}]_c$ is raised above 1 mM, and is effectively blocked at 10 mM $[Mg^{2+}]_c$ (Lamb and Stephenson, 1991, 1992, 1994). The fact that maximal activation of the DHPRs cannot open the RyR1s/α-RyRs pores in the presence of 10 mM $[Mg^{2+}]_c$ strongly suggests that the inhibition exerted by Mg^{2+} on the RyR1s/α-RyRs must be removed (Lamb and Stephenson, 1991, 1994) before pores can open. Based on these experiments Lamb and Stephenson proposed that activation of DHPRs by depolarization of the t-system membrane induces a 10–20-fold decrease in the affinity of Mg^{2+} binding to sites on RyR1s/α-RyRs that inhibit the opening of the RyR1s/α-RyRs (Lamb and Stephenson, 1991, 1994, Stephenson 1996, 2006; Stephenson et al., 1998; Lamb, 2000, 2002a, 2002b; Laver 2018; and references therein).

Support for voltage- and implicitly DHPR-activation-dependent change in $[Mg^{2+}]$-induced inhibition of SR–Ca^{2+} release observed in mechanically skinned muscle fibers has been further obtained from experiments on isolated triads (Ritucci and Corbett, 1995) and voltage-clamped cut fibers of frog (Jacquemond and Schneider, 1992) and rat (Jóna et al., 2001). For example, Jóna et al. (2001) reported a 10-fold decrease in the apparent affinity of Mg^{2+} binding to sites on rat RyR1s when the membrane potential of the muscle fiber changed from normal polarization to full depolarization.

Thus, one can envisage that a sudden reduction of inhibition at the low-affinity Ca^{2+}/Mg^{2+} I1 sites of *${}^{c}RyR1s$* in a couplon caused by activation of the DHPRs, could initiate a positive feedback loop that increases Ca^{2+} leak into the JS, raising $[Ca^{2+}]_{js}$ in the micromolar range that subsequently activates more *${}^{c}RyR1s$* at their A-sites to open their pores, which in turn, further increases the Ca^{2+} leak/flux into the JS.

For proof of principle, it is assumed, in the first instance that (1) couplons are initially equilibrated under resting conditions [$[Ca^{2+}]_{js}$ = 203 nM, $[Ca^{2+}]_c$ = 67 nM, $[Ca^{2+}]_{SR}$ = 400 µM, $[Mg^{2+}]_{js}$ = 1 mM, $[M_m{}^{+}]_{js}$ = 150 mM], (2) $[Ca^{2+}]_c$, $[Mg^{2+}]_{js}$, and $[M_m{}^{+}]_{js}$ do not change following maximal activation of the DHPRs, (3) Ca^{2+} binding to calsequestrin is in rapid equilibrium with $[Ca^{2+}]_{SR}$ and does not affect RyR1 function, (4) there is no putative activation of the *${}^{nc}RyR1s$* by their neighboring *${}^{c}RyR1s$* when the latter become activated by DHPR activation, and (5) the SR–Ca^{2+} pump

is blocked. For modeling, the kinetics of activation of the $^{c}RyR1s$ it was considered that the functional state of the RyR1s is determined by the level of ion occupancy at the Ca^{2+} activation A-sites and the low-affinity Ca^{2+}/Mg^{2+} inhibition I1 sites on the four protomers of a RyR1 at time t, and that the binding rate constants of Ca^{2+}, Mg^{2+}, and M_m^{+} to RyR1 sites (k_{on}) are diffusion-limited, with k_{on} = 4 × 10^8 M^{-1} s^{-1}, like those for BAPTA (4.5 × 10^8 M^{-1} s^{-1} for Ca^{2+}; Naraghi, 1997) and ATP (4 × 10^8 $M^{-1}s^{-1}$ for Mg^{2+}; Pecoraro et al., 1984). The dissociation rate constants (k_{off}) of Ca^{2+}, Mg^{2+}, and M_m^{+} from specific RyR1 sites were then obtained from the equilibrium dissociation constants (K_D) listed in Table 1 ($k_{off} = k_{on}\ K_D$), which were derived from experimental results as described in Appendix 1.

Eq. 11, where $[Ca^{1p}A(t)]/[^{1p}A_{Total}]and[Mg^{1p}A(t)]/[^{1p}A_{Total}]$ represent normalized levels of Ca^{2+}- and Mg^{2+}- occupancy on the protomeric A-sites in the couplon at time t and $^{4p}K_{in}$ is the Ca^{2+}/Mg^{2+} equilibrium dissociation constant from I1 sites on protomers of $^{c}RyR1s$, describes the time dependence of the open probability of one $^{nc}RyR1$ and one $^{c}RyR1$ $[^{nc}P_O\,(t) + {}^{c}P_O\,(t)]$ when the system is not at steady-state and is derived from Eq. A27 in Appendix 1 with parameter values in Table 1:

$$
\begin{aligned}
{}^{nc}P_0(t) + {}^{c}P_0(t) = &\left(0.56 + \frac{0.35}{\left(1 + \frac{250\mu M}{[Ca^{2+}(t)]_{SR}}\right)}\right) \times \\
&\left(1 - \frac{[Ca^{1p}A(t)]}{[^{1p}A_{Total}]} - \frac{[Mg^{1p}A(t)]}{[^{1p}A_{Total}]}\right) + \\
&0.963\frac{[Ca^{1p}A(t)]}{[^{1p}A_{Total}]})^4 \times \\
&\left(\left(1 + \frac{\left([CaMg(t)]_{js}\right)^2}{(0.05\mathrm{mM})^2}\right)^{-1} + \left(1 + \frac{\left([CaMg(t)]_{js}\right)^4}{\left({}^{4p}K_{in}\right)^4}\right)^{-1}\right)
\end{aligned}
\tag{11}
$$

Note that as indicated in Table 1, $^{4p}K_{in}$ = 0.05 mM when DHPRs are not activated and 1.5 mM when DHPRs are maximally activated.

Time-dependent changes of specific properties associated with the functional state of $^{c}RyR1s$ and $^{nc}RyR1s$ in a couplon following perturbations induced by sudden 30-fold rise in apparent dissociation constant at the inhibitory Ca^{2+}/Mg^{2+} I1 sites of $^{c}RyR1s$ were obtained by numerically solving the set of four differential Eqs. 12, 13, 14, and 15 in $[Ca^{2+}(t)]_{js}$, $[Ca^{1p}A(t)]/[^{1p}A_{Total}]$, $[Mg^{1p}A(t)]/[^{1p}A_{Total}]$, and $[Ca^{2+}(t)]_{SR}$ with Wolfram Mathematica online (program scripts provided in Data S1, S2, S3, S4, S5, and S6).

Eq. 12 is derived from Eqs. 1, 8, 9, and 11 where Ca^{2+} − inflow$(t) = k_{SRJS}\left([Ca^{2+}(t)]_{SR} - [Ca^{2+}(t)]_{js}\right)$, Ca^{2+} − outflow $(t) = k_{diff}\left([Ca^{2+}(t)]_{js} - 0.067\mu M\right)$, and $P_{A0}(t) = ((0.56+\frac{0.35}{1+250\mu M/[Ca^{2+}(t)]_{SR}})(1-\frac{[Ca^{1p}A(t)]}{[^{1p}A_{Total}]}-\frac{[Mg^{1p}A(t)]}{[^{1p}A_{Total}]}) + 0.963\frac{[Ca^{1p}A(t)]}{[^{1p}A_{Total}]})^4$ and describes the time dependence of $[Ca^{2+}(t)]_{js}$ immediately after the sudden 30-fold rise in $^{4p}K_{in}$ from 0.05 to 1.5 mM:

$$
\begin{aligned}
&d[Ca^{2+}(t)]_{js}/dt = Ca^{2+} - inflow(t) - Ca^{2+} - outflow(t) = \\
&1,964ms^{-1} \times \left([Ca^{2+}(t)]_{SR} - [Ca^{2+}(t)]_{js}\right)({}^{nc}P_0(t) + {}^{c}P_0(t)) - \\
&(14ms^{-1} + 7,216ms^{-1}P_{A0}(t)) \times \left([Ca^{2+}(t)]_{js} - 0.067\mu M\right) = \\
&1,964ms^{-1}\left([Ca^{2+}(t)]_{SR} - [Ca^{2+}(t)]_{js}\right)((0.56 + \frac{0.35}{1 + \frac{250\mu M}{[Ca^{2+}(t)]_{SR}}}) \\
&\left(1 - \frac{[Ca^{1p}A(t)]}{[^{1p}A_{Total}]} - \frac{[Mg^{1p}A(t)]}{[^{1p}A_{Total}]}\right) + 0.963\frac{[Ca^{1p}A(t)]}{[^{1p}A_{Total}]}\Bigg)^4 \times \\
&\left(\frac{1}{1 + \frac{\left([CaMg(t)]_{js}\right)^2}{(0.05mM)^2}} + \frac{1}{1 + \frac{\left([CaMg(t)]_{js}\right)^4}{(1.5mM)^4}}\right) - (14ms^{-1} + 7,216ms^{-1} \times \\
&\left(\left(0.56 + \frac{0.35}{1 + \frac{250\mu M}{[Ca^{2+}(t)]_{SR}}}\right)\left(1 - \frac{[Ca^{1p}A(t)]}{[^{1p}A_{Total}]} - \frac{[Mg^{1p}A(t)]}{[^{1p}A_{Total}]}\right) + \right. \\
&\left. 0.963\frac{[Ca^{1p}A(t)]}{[^{1p}A_{Total}]}\right)^4)\left([Ca^{2+}(t)]_{js} - 0.067\mu M\right)
\end{aligned}
\tag{12}
$$

Eqs. 13 and 14 are derived from Eqs. A23 and A24 in Appendix 1, respectively, considering that $[M_m^{+}]_{js}$ = 150 mM and K_{Mm} = 172.1 mM (Table 1) and describe the time-dependent changes of the normalized levels of Ca^{2+}- and Mg^{2+}- occupancy at the protomeric A-sites in the couplon:

$$
\begin{aligned}
&d\left(\frac{[Ca^{1p}A(t)]}{[^{1p}A_{Total}]}\right)/dt = 0.2273\ \mu M^{-1}ms^{-1}[Ca^{2+}(t)]_{js} \times \\
&\left(1 - \frac{[Ca^{1p}A(t)]}{[^{1p}A_{Total}]} - \frac{[Mg^{1p}A(t)]}{[^{1p}A_{Total}]}\right) - \\
&0.028ms^{-1}\frac{[Ca^{1p}A(t)]}{[^{1p}A_{Total}]}\Bigg)
\end{aligned}
\tag{13}
$$

$$
\begin{aligned}
&d\left(\frac{[Mg^{1p}A(t)]}{[^{1p}A_{Total}]}\right)/dt = 227.3ms^{-1} \times \\
&\left(1 - \frac{[Ca^{1p}A(t)]}{[^{1p}A_{Total}]} - \frac{[Mg^{1p}A(t)]}{[^{1p}A_{Total}]}\right) - \\
&12.26ms^{-1}\left(1 + \frac{[Ca(t)_{SR}]}{346.6\mu M}\right)\frac{[Mg^{1p}A(t)]}{[^{1p}A_{Total}]}
\end{aligned}
\tag{14}
$$

Finally, Eq. 15 describes the time course of $[Ca^{2+}]_{SR}$ and was derived from Eq. 10 after ${}^{nc}P_O(t) + {}^{c}P_O(t)$ was substituted with the expression given in Eq. 11:

$$d[Ca^{2+}(t)]_{SR}/dt = -7.25ms^{-1}\left([Ca^{2+}(t)]_{SR} - [Ca^{2+}(t)]_{js}\right) \times \left((0.56 + \frac{0.35}{1 + 250\mu M/[Ca^{2+}(t)]_{SR}}\right)\left(1 - \frac{[Ca^{lp}A(t)]}{[^{lp}A_{Total}]} - \frac{[Mg^{lp}A(t)]}{[^{lp}A_{Total}]}\right) + 0.963\frac{[Ca^{lp}A(t)]}{[^{lp}A_{Total}]}^4\left(\frac{1}{1 + \frac{\left([CaMg(t)]_{js}\right)^2}{(0.05mM)^2}} + \frac{1}{1 + \frac{\left([CaMg(t)]_{js}\right)^4}{\left({}^{4p}K_{in}\right)^4}}\right) \times \frac{\left(1 + \frac{[Ca^{2+}(t)]_{SR}}{1mM}\right)^2}{37.1 + \left(1 + \frac{[Ca^{2+}(t)]_{SR}}{1mM}\right)^2} \quad (15)$$

Fig. 1 A shows the predicted timecourse of $[Ca^{2+}(t)]_{js}$ after the sudden reduction of inhibition at the low-affinity Ca^{2+}/Mg^{2+} I1 sites of ${}^{c}RyR1s$ in a couplon caused by maximal activation of the DHPRs in a mammalian muscle fiber. At time zero, ${}^{4p}K_{in}$ suddenly rises from 0.05 to 1.5 mM in the ${}^{c}RyR1s$ of a couplon induced by the simultaneous maximal activation of the associated DHPRs (as considered in Eq. 12). Mg^{2+} dissociates very quickly from the Ca^{2+}/Mg^{2+} I1 sites of ${}^{c}RyR1s$ with a rate constant k_{off} in the order of 6×10^5 s^{-1} (4×10^8 M^{-1} s^{-1} × 1.5 mM), ensuring the swift reduction of inhibition at the I1 sites of ${}^{c}RyR1s$ within few µs that, in turn, induces a 581-fold rise of $[Ca^{2+}]_{js}$ from 0.203 nM to 70 µM within 0.5 ms (see inset in Fig. 1 A). The very large rise in $[Ca^{2+}]_{js}$ facilitates the rapid displacement of Mg^{2+} from the A-sites on all RyR1 protomers in the couplon so as to increase the Ca^{2+} occupancy at the A-sites from 14.6% at rest to 97% within 2 ms following the DHPR-induced rise in ${}^{4p}K_{in}$ (Fig. 1 B). With the SR Ca^{2+} pump blocked, there is a rapid SR Ca^{2+} depletion such that $[Ca^{2+}]_{SR}$ decreases 89% of the initial value after 20 ms and 99.2% after 500 ms of maximal DHPR activation (Fig. 1 C). Meanwhile, the open probability of the DHPR-coupled RyR1s (${}^{c}P_o(t)$) shoots up from 1.2×10^{-8} to 0.62 within 4 ms (while ${}^{nc}P_o(t)$ only rises from 4.8×10^{-6} to 1.7×10^{-3}) causing the SR Ca^{2+} permeability to increase from 0.0095 to 1,200 ms^{-1} in 3.5 ms (inset in Fig. 1 C). The large increase in ${}^{c}P_o(t)$ supports an SR Ca^{2+} flux into the cytosol at large with a peak of 61.0 µM ms^{-1} (expressed as Ca^{2+} released per volume of cytoplasmic water) after 1.8 ms following excitation (Fig. 1 D). Note that the maximal rate of SR Ca^{2+} release into the cytosol can exceed 100 µM ms^{-1} if all ${}^{c}RyR1s$ in the couplon become activated and induce the simultaneous activation of all adjacent ${}^{nc}RyR1s$ as suggested by experiments where two or more RyR1s that are physically connected when incorporated in lipid bilayers can open and close simultaneously (Marx et al., 1998; Laver et al., 2004; Porta et al., 2012).

The inset in Fig. 1 D shows the time course of the SR Ca^{2+} flux into the cytosol when the SR Ca^{2+} pump is very active, returning 200 µM Ca^{2+} (relative to SR volume) ms^{-1} (1 – $[Ca^{2+}t)]_{SR}$/400 µM) that would fill the empty SR in a resting fiber in a matter of 200 ms. $[Ca^{2+}]_{SR}$ decreases by 82.5% of its initial value after 20 ms of maximal stimulation and then equilibrates at 59.5 µM. The reduced Ca^{2+} gradient across the SR membrane causes the SR Ca^{2+} release flux to drop to a lower level without the pump having any significant effect on the peak of the SR Ca^{2+} release flux into the cytosol (inset Fig. 1 D). Thus, as the simulation shows, the SR Ca^{2+} flux will decrease from an early peak to a lower level at constant stimulation when the SR-Ca^{2+} release flux exceeds the Ca^{2+} return flux by the SR-Ca^{2+} pump. The reduction in the Ca^{2+} flux entering the JS further reduces $[Ca^{2+}]_{js}(t)$, causing ${}^{c}P_O$ and SR membrane permeability to decrease, the outcome resembling a Ca^{2+} inactivation process of RyR1s.

According to simulations shown in Fig. 2, $[Ca^{2+}]_{js}(t)$ and SR Ca^{2+} release flux are determined by the fraction of DHPR-activated ${}^{c}RyRIs$. Consequently, the charge movement associated with DHPR activation of ${}^{c}RyRIs$ is a measure of DHPR-activated ^{c}RyR1s. The close association between SR Ca^{2+} release and fraction of DHPR-activated ${}^{c}RyRIs$ shown in Fig. 2 will therefore result in voltage control of Ca^{2+}-release through voltage-dependent DHPR-activation.

The proposed mechanism of DHPR-dependent activation of Ca^{2+} release is robust in the presence of Ca^{2+} buffers and when the SR Ca^{2+} content is reduced

Let us assume that 10 mM of a fast Ca^{2+} buffer such as BAPTA is present in the cytosol at large in a resting mammalian muscle fiber at the time of stimulation. The Ca^{2+}-bound form of BAPTA (CaBAPTA^{2-}) carries two negative charges suggesting that the diffusiveness of CaBAPTA^{2-} across a negatively charged JS/cytosol barrier is orders-of-magnitude smaller compared with that of Ca^{2+} as it is the case for CaEGTA^{2-}, discussed above. The very large difference between the diffusiveness of Ca^{2+} and CaEGTA^{2-} or CaBAPTA^{2-} ensures that a steady Ca^{2+} leak into the JS generates a $[Ca^{2+}]_{js}$–$[Ca^{2+}]_c$ difference that is about the same at steady-state in the absence as in the presence of mM BAPTA or EGTA.

The association rate constant of Ca^{2+} to BAPTA^{4-} (${}^{BAPTA}k_{on}$) and the dissociation rate constant of Ca^{2+} from CaBAPTA^{2-} (${}^{BAPTA}k_{off}$) were taken as 4.5×10^8 M^{-1} s^{-1} (= 0.45 µM^{-1} ms^{-1}) and 79 s^{-1} (= 0.079 ms^{-1}), respectively, based on the study of Naraghi (1997) conducted at pH 7.2 and 22°C. Consequently, the dissociation equilibrium constant for BAPTA, ${}^{BAPTA}K_D = {}^{BAPTA}k_{off}/{}^{BAPTA}k_{on}$ is 0.1756 µM and the concomitant changes in $[Ca^{2+}(t)]_{js}$, $[CaBAPTA]_{js}$ ($[CaBAPTA\ (t)]_{js}$) and $[BAPTA_{free}]_{js}$ (10,000 µM–$[CaBAPTA(t)]_{js}$) are governed by Eqs. 16 and 17:

$$d[CaBAPTA(t)]_{js}/dt = 0.45\mu M^{-1}ms^{-1}[Ca^{2+}(t)]_{js} \times \left(10,000\mu M - [CaBAPTA(t)]_{js}\right) - 0.079ms^{-1} \times [CaBAPTA(t)]_{js} = -0.079ms^{-1}[CaBAPTA(t)]_{js} \times \left(1 + 5.696\mu M^{-1}[Ca^{2+}(t)]_{js}\right) + 4,500ms^{-1}[Ca^{2+}(t)]_{js} \quad (16)$$

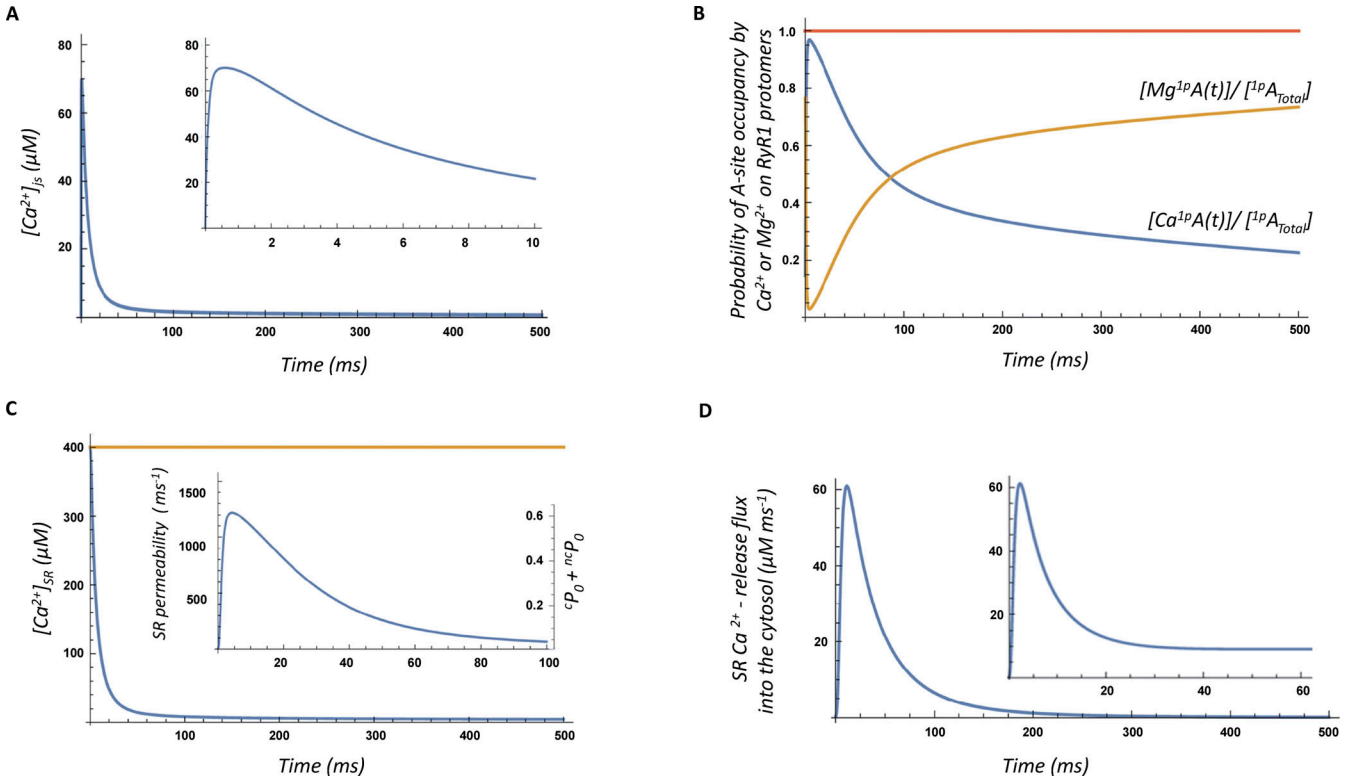

Figure 1. **Predicted time course of $[Ca^{2+}(t)]_{js}$ and Ca^{2+}-release properties of mammalian muscle fibers following sudden, DHPR-activation dependent reduction of Mg^{2+} inhibition at Ca^{2+}/Mg^{2+} I1 sites of $^{c}RyR1s$. (A)** Time course of $[Ca^{2+}(t)]_{js}$ on 0.5 s and an expanded time scale in the inset, following maximal DHPR activation in a couplon at $t = 0$. The peak of $[Ca^{2+}(t)]_{js}$ exceeds 70 μM due to the massive increase in the junctional SR permeability for Ca^{2+} and the limited diffusiveness of Ca^{2+} across the JS/cytosol barrier. **(B)** Time course of Ca^{2+} and Mg^{2+} occupancy of individual/protomeric A-sites of RyR1s in a couplon. **(C)** Time course of SR Ca^{2+} depletion ($[Ca^{2+}(t)]_{SR}$), changes in junctional SR permeability for Ca^{2+} (k_{SRJS}) (inset, lefthand side vertical scale), and open probability of one DHPR-coupled RyR1 ($^{c}P_O(t)$) and one DHPR-noncoupled RyR1 ($^{nc}P_O(t)$) in the JS (inset, righthand side vertical scale). Before stimulation $^{nc}P_O(t)/(^{c}P_O(t)) \approx 400$ and decreases to ≈ 0.0027 at the peak of SR permeability for Ca^{2+}. **(D)** Time course of SR Ca^{2+}—release flux into the cytosol (μM Ca^{2+} released per volume of cytosol per ms). The inset depicts the predicted SR Ca^{2}-release flux into the cytosol if the SR Ca^{2+} pump was very active, returning 200 μM Ca^{2+} (relative to SR volume) ms^{-1} $(1 - [Ca^{2+}(t)]_{SR}/400\ \mu M)$, which would fill the empty SR in a non-stimulated "fiber" in <200 ms. Note that the peak SR Ca^{2+} efflux is hardly affected when the SR Ca^{2+} pump is active. The orange lines in B and C show the maximum probability of A-site occupancy (1.0) and $[Ca^{2+}(0)]_{SR}$, respectively.

$$d[Ca^{2+}(t)]_{js}/dt = 1,964 ms^{-1}\left([Ca^{2+}(t)]_{SR} - [Ca^{2+}(t)]_{js}\right) \times (^{nc}P_0(t) + {}^{c}P_0(t)) + 0.079 ms^{-1}[CaBAPTA(t)]_{js} \times \left(1 + 5.696 \mu M^{-1}[Ca^{2+}(t)]_{js}\right) - 4,500 ms^{-1}[Ca^{2+}(t)]_{js} - (14 ms^{-1} + 7,216 ms^{-1}P_{A0}(t))\left([Ca^{2+}(t)]_{js} - 0.067 \mu M\right) \quad (17)$$

where $(^{nc}P_0(t) + {}^{c}P_0(t))$ is given by Eq. 11 and $P_{A0}(t) = (0.56 + (0.35/(1 + 250\mu M/[Ca^{2+}(t)]_{SR})) \times (1 - \frac{[Ca^{1p}A(t)]}{[^{1p}A_{Total}]} - \frac{[Mg^{1p}A(t)]}{[^{1p}A_{Total}]}) + 0.963\frac{[Ca^{1p}A(t)]}{[^{1p}A_{Total}]})^{4}$.

The time course of $[Ca^{2+}(t)]_{js}$ and that of the other parameters associated with the functional state of $^{c}RyR1s$ and $^{nc}RyR1s$ in couplons following the sudden DHPR-activation–dependent decreased inhibition at the I1 sites of $^{c}RyR1s$ in the presence of 10 mM BAPTA was predicted by numerically solving the system of Eqs. 13, 14, 15, 16, and 17 with Wolfram Mathematica online for two sets of conditions when the "fiber" was at rest, before being stimulated. In one case, the values of the parameters in the fiber at rest were same as those in the absence of 10 mM BAPTA ($[Ca^{2+}]_{SR}$ = 400 μM, $[Ca^{2+}]_{js}$ = 203 nM, $[Ca^{2+}]_c$ = 67 nM, $[Mg^{2+}]_{js}$ = 1 mM and $[M_m{}^{+}]_{js}$ = 150 mM). In the other case, the SR was severely depleted of Ca^{2+} with $[Ca^{2+}]_{SR}$ = 100 μM, but $[Ca^{2+}]_{js}$, $[Mg^{2+}]_{js}$ and $[M_m{}^{+}]_{js}$ were kept the same as in the first case to permit more direct examination of the effect of SR Ca^{2+} depletion on the activation of SR Ca^{2+} release. The marked reduction in the Ca^{2+} leak into the JS at rest caused by the lower luminal SR Ca^{2+} can only sustain a difference of ∼5 nM between $[Ca^{2+}]_{js}$ and $[Ca^{2+}]_c$. Therefore, $[Ca^{2+}]_c$ at rest was deemed to be 198 nM (= 203–5 nM) in this case. All other assumptions detailed in the paragraph prior to the description of Eq. 11 were also adopted for computing the time course of Ca^{2+} release in the presence of 10 mM BAPTA.

When the SR is endogenously loaded with Ca^{2+} at the time of DHPR activation, the $[Ca^{2+}(t)]_{js}$ response is slightly delayed in 10 mM BAPTA (Fig. 3 A and inset) than in the absence of BAPTA (Fig. 1 A and inset), but it reaches the same peak (70 μM) after 3 ms with BAPTA and after 0.6 ms without BAPTA. The SR Ca^{2+}-release flux into the cytosol (inset in Fig. 3 B) reaches a peak that is just a fraction higher in the presence than in the absence of BAPTA (61.5 versus 61.0 μM per volume of cytosol ms^{-1}, respectively) due in part to the slightly delayed decrease in $[Ca^{2+}(t)]_{SR}$ (Fig. 3 B).

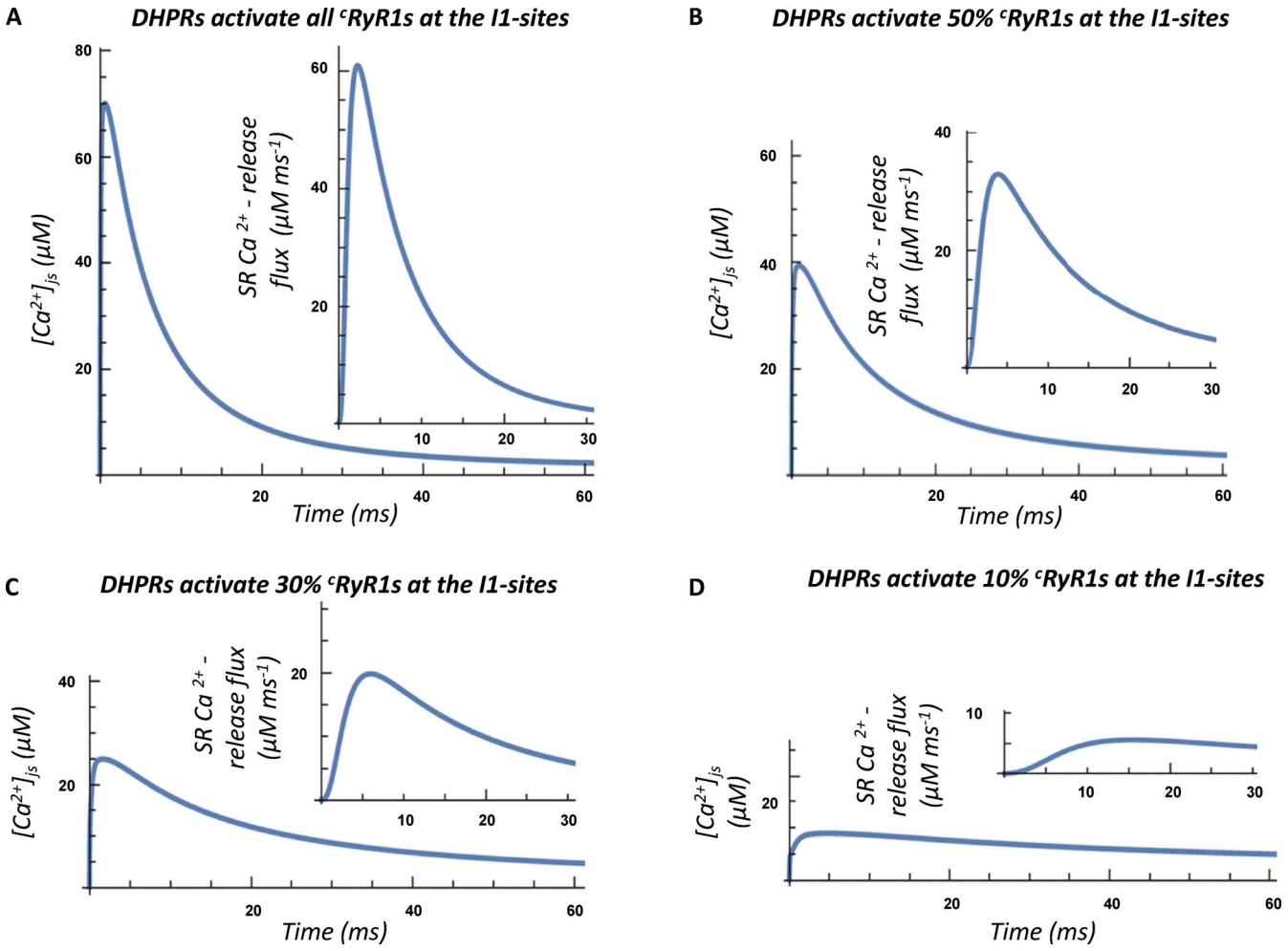

Figure 2. **Ca^{2+}-release dependence on levels of DHPR-activation. (A–D)** Predicted time course of $[Ca^{2+}(t)]_{js}$ and *SR* Ca^{2+}-release flux (t) at the maximal level of DHPR-activation and when the percentage of *ᶜRyR1s* with DHPR-activation-dependent reduction of inhibition at the I1 sites is decreased (B) to 50%, (C) to 30%, and (D) to 10%. The graded reduction of Ca^{2+} release when the fraction of DHPR-activated *ᶜRyR1s* is decreased at lower levels of DHPR-activation shows that the regenerative Ca^{2+} release is under DHPR control and implicitly under voltage control.

In contrast, when the SR is severely depleted of Ca^{2+} at time of maximum DHPR activation ($[Ca^{2+}(0)]_{SR}$ = 100 μM) in 10 mM BAPTA, there is a relatively long delay after stimulation (~35 ms) for $[Ca^{2+}(t)]_{js}$ to reach the threshold for producing a spike (Fig. 3 C trace a). The inset in Fig. 3 C (trace b) displays the time course of $[Ca^{2+}(t)]_{js}$ when $[Ca^{2+}]_{SR}$ (0) = 100 μM in the absence of BAPTA, showing that the presence of BAPTA is responsible for the delay, but does not affect $[Ca^{2+}(t)]_{js}$ peak height. Similarly, in the presence of 10 mM BAPTA, there is a delay before $[Ca^{2+}]_{SR}$ starts to decrease more rapidly (Fig. 3 D) and before SR Ca^{2+}-release flux into the cytosol reaches its peak (inset in Fig. 3 D). When $[Ca^{2+}]_{SR}(0)$ = 100 μM in the absence of BAPTA, $[Ca^{2+}]_{SR}$ decreases rapidly without delay after stimulation, while the SR Ca^{2+}-release flux reaches the same peak height as in the presence of BAPTA 9.1 ms after stimulation (Fig. 3 E). Significantly, if 10 mM BAPTA is replaced with 10 mM EGTA, which binds and releases Ca^{2+} slower than BAPTA ($^{EGTA}k_{on}$ = 0.00167 μM^{-1} ms^{-1}, $^{EGTA}k_{off}$ = 0.00031 ms^{-1}) and the SR is severely depleted of Ca^{2+} at time of DHPR activation, the spike in $[Ca^{2+}(t)]_{js}$ occurs without delay and the SR Ca^{2+}-release flux starts rising within 2 ms (Data S4).

There is an apparent discrepancy between the ~35-ms delay predicted by the model for the onset of $[Ca^{2+}]_{SR}$ decrease after stimulation in the presence of 10 mM BAPTA when $[Ca^{2+}]_{SR}$ (0) = 100 μM (Fig. 3 D) and the absence of such delay in experiments of Olivera and Pizarro (2018), who measured the time course of $[Ca^{2+}]_{SR}$ in frog muscle fibers after stimulation following SR Ca^{2+} depletion to $[Ca^{2+}]_{SR}$ = 100 μM in the presence of 20 mM BAPTA (see Fig. 3 B in their paper). The depletion of $[Ca^{2+}]_{SR}$ in these experiments occurred after the addition of 20 mM BAPTA (2.04 mM $CaBAPTA^{2-}$ and 17.96 mM $BAPTA^{4-}$ at 20 nM $[Ca^{2+}]$ with Cs^+ as counterion) to an internal Cs-based solution of ~150 mM ionic strength. The addition of 20 mM BAPTA would have increased the overall ionic strength of the internal solution by about 186–336 mM, which, in turn, would have raised K_{in} to ≥2.5 mM according to measurements of Laver et al. (2004) using Cs-based solutions of similar ionic strength (see their Fig. 1 and Table 1). A greater K_{in} would reduce inhibition at the Ca^{2+}/Mg^{2+} I1 sites of non-DHPR-coupled RyRs at constant cytosolic $[Mg^{2+}]$

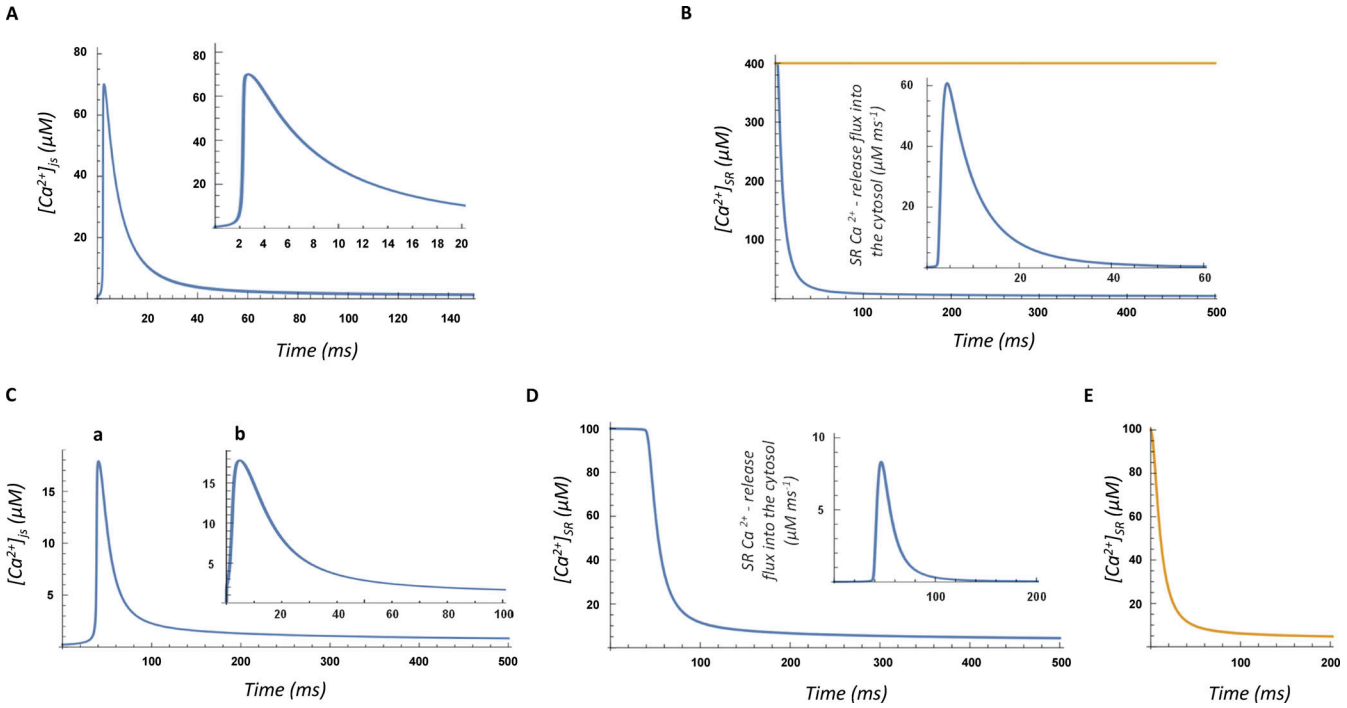

Figure 3. **Predicted time course of parameters associated with Ca^{2+} release in mammalian muscle fibers following sudden, DHPR-activation-dependent reduction of Mg^{2+} inhibition at Ca^{2+}/Mg^{2+} I1-sites of $^{c}RyR1s$ in the presence of BAPTA. (A and B)** Predicted time course of $[Ca^{2+}(t)]_{js}$, $[Ca^{2+}]_{SR}$, and SR Ca^{2+} release flux into the cytosol upon DHPR-activation-dependent reduction of Mg^{2+} inhibition at Ca^{2+}/Mg^{2+} I1 sites of $^{c}RyR1s$ in the presence of 10 mM BAPTA for ionic conditions at rest that are same as in the absence of BAPTA and SR was loaded with Ca^{2+} at endogenous level ($[Ca^{2+}]_{SR}$ = 400 μM) prior to stimulation. The orange line in B shows $[Ca^{2+}(0)]_{SR}$. **(C and D)** Predictions for severely depleted SR of Ca^{2+} at the time of stimulation ($[Ca^{2+}]_{SR}(0)$ = 100 μM) in the presence of 10 mM BAPTA. The cationic conditions in the JS at time of stimulation for trace a in C and for both traces in D were the same as those at rest used for panel A and B to ensure that the Ca^{2+} buffering capacity of 10 mM BAPTA in the JS was same at time of stimulation when the SR was endogenously loaded or severely depleted of Ca^{2+}. For comparison purposes, trace b in C shows the time course of $[Ca^{2+}(t)]_{js}$ when $[Ca^{2+}]_{SR}(0)$ = 100 μM in the absence of BAPTA. The inset in D shows the SR Ca^{2+}-release flux into the cytosol when the SR at rest is severely depleted of Ca^{2+}. **(E)** Simulation of the time course of $[Ca^{2+}]_{SR}$ in a muscle fiber with depleted SR at the time of stimulation ($[Ca^{2+}]_{SR}(0)$ = 100 μM) in a solution of elevated ionic strength that increased K_{in} (and $^{4p}K_{in}$) from 0.05 to 0.25 mM in the presence of 20 mM BAPTA and 20 nM $[Ca^{2+}]_c$ (see text). The increased K_{in} reduces inhibition at the Ca^{2+}/Mg^{2+} I1 sites at rest and increases the SR Ca^{2+} leak into the JS despite the reduction in $[Ca^{2+}]_{SR}$ from 400 to 100 μM causing $[Ca^{2+}]_{js}$ to rise to 1.6 μM at time of stimulation. Under these conditions, the sudden 30-fold DHPR-activation-induced rise of $^{4p}K_{in}$ to 7.5 mM causes SR Ca^{2+} release with no significant delay, despite severe SR Ca^{2+} depletion.

(~1 mM). Consequently, P_{IO} in the muscle fibers at rest would have risen considerably in the experiments of Olivera and Pizarro (2018) after the addition of 20 mM BAPTA and would have caused the SR Ca^{2+} leak into the JS and the rest of the cytosol to rise in spite of a gradual decrease of $[Ca^{2+}]_{SR}$ from 400 to 100 μM, as was indeed reported by Olivera and Pizarro (2018). As a result, $[Ca^{2+}]_{js}$ at time of stimulation would have been sizably greater in the experiments of Olivera and Pizarro (2018) than 203 nM considered in the model simulation shown in Fig. 3 D. In the model simulation shown in Fig. 3 E, a rise in K_{in} (and $^{4p}K_{in}$) from 0.05 to 0.25 mM (rather than to 2.5 mM) caused $[Ca^{2+}]_{js}$ to rise to 1.6 μM when $[Ca^{2+}]_{SR}$ = 100 μM at the time of stimulation and produce a prompt decline of $[Ca^{2+}]_{SR}$ upon stimulation, as reported by Olivera and Pizarro (2018) in their experiments (Data S6). Thus, apparent controversies between experimental observations and model-based predictions could be simply due to differences between perceived values of parameters at the time of stimulation in experimental settings and actual values used in model-based simulations.

It is also important to mention that the proposed mechanism of Ca^{2+} release predicts that maximal DHPR activation induces a regenerative Ca^{2+} release spike even when $[Ca^{2+}]_{SR}$ is reduced to 10 μM in the presence of 10 mM BAPTA in the JS, and $[Ca^{2+}]_{js} \approx [Ca^{2+}]_c$ = 0.10 μM. In this case, according to simulation, $[Ca^{2+}(t)]_{js}$ reaches 1.3 μM after 12.9 s of continuous stimulation if the DHPRs do not become inactivated and the diffusiveness of BAPTA across the JS/cytosol barrier under resting conditions is negligible over this period of 12.9 s (Data S3).

Taken together, these results highlight the robustness of the proposed hypothesis.

Overview of the putative mechanism of Ca^{2+} release in skeletal muscle

Central to the proposed hypothesis is the presence of a diffusional JS/cytosol barrier that supports an elevated $[Ca^{2+}]_{js}$ relative to $[Ca^{2+}]_c$ in the presence of a small Ca^{2+} leak into the JS. Sudden activation of DHPRs on DHPR-coupled RyR1s/α-RyRs induces a sudden, localized disturbance at the low-affinity Ca^{2+}/Mg^{2+} I1-inhibitory sites of the coupled RyR1s/α-RyRs

by allosteric regulation. The signal between the sites of physical interaction of the four DHPRs with the four protomers of the $^{c}RyR1$ and the base of the RyR1, where the I1-sites are located is possibly transmitted via long levers that provide long-range allosteric pathway within the cytosolic shell of the RyR1s as recently proposed by Nayak et al. (2024). The disturbance at the I1 sites raises the Ca^{2+}/Mg^{2+} equilibrium dissociation constant causing a small fraction of DHPR-activated $^{c}RyR1s$ to open their pores at the prevalent $[Ca^{2+}]_{js}$ when inhibition at their I1 sites is eased. Consequently, the Ca^{2+} flux/leak into the JS rapidly rises and the presence of the JS/cytosol diffusional barrier facilitates the rise of $[Ca^{2+}]_{js}$ that starts a regenerative Ca^{2+} activation process confined to the fraction of voltage-activated coupled RyR1s/α-RyRs. The rising $[Ca^{2+}]_{js}$ causes Ca^{2+} to displace Mg^{2+} at the A-sites of RyR1s/α-RyRs leading to full activation of the DHPR-activated fraction of RyR1s/α-RyRs. As shown in Fig. 2, $[Ca^{2+}]_{js}(t)$ and SR Ca^{2+} release flux are governed by the fraction of DHPR-activated $^{c}RyR1s$, which ensures voltage control of Ca^{2+}-release through voltage-dependent DHPR-activation. Increased Ca^{2+} diffusiveness across the JS/cytosol barrier by a mechanism analogous to that that opens floodgates in a reservoir when the level of water in the reservoir exceeds a certain level greatly enhances the Ca^{2+} flux from the JS into the bulk cytosol. Deactivation or inactivation of DHPRs rapidly reinstates inhibition at the Ca^{2+}/Mg^{2+} I1 sites of the DHPR-coupled RyR1s/α-RyRs in the presence of 1 mM $[Mg^{2+}]_{js}$. Consequently, the vast majority of DHPR-coupled RyR1s/α-RyRs close, Ca^{2+} leak into the JS and $[Ca^{2+}]_{js}$ declines, and Mg^{2+} binds to the A-sites of all RyRs in the couplons, further reducing the size of the Ca^{2+} leak into the JS and $[Ca^{2+}]_{js}$.

Points of caution

Essential to the proposed model for the mechanism of Ca^{2+} release in skeletal muscle by DHPRs is the existence of a diffusional barrier between the narrow space, where cytosolic Ca^{2+} and Mg^{2+} regulatory sites are located on RyRs, and the rest of the cytosol. There is evidence that this barrier displays low diffusiveness for Ca^{2+} at low $[Ca^{2+}]_{js}$ (Barclay and Launikonis, 2022) and even a much lower diffusiveness (by orders of magnitude) for divalent anions such as $CaEGTA^{2-}$ and $EGTA^{2-}$ (as detailed in this paper), features that are typical of cation exchange membranes (Tekinalp et al., 2023). Such membranes carry fixed negative charges that severely reduce the diffusiveness of divalent anions relative to cations (Tekinalp et al., 2023). The extremely low diffusiveness of anions ensures that little exchange takes place between anions in the JS and those in the rest of the cytosol for relatively short periods of time after stimulation. As shown by simulations of the proposed model, the orders-of-magnitude lower diffusiveness of the barrier for divalent anions than for Ca^{2+} allows Ca^{2+} induced Ca^{2+}-release to produce a spike following stimulation even in the presence of large concentrations of negatively charged Ca^{2+} buffers like $CaEGTA^{2-}/EGTA^{2-}$ or $CaBAPTA^{2-}/BAPTA^{4-}$. The precise nature of the barrier is not known, although it is likely to incorporate proteins present in the JS including DHPRs, RyRs, JPHs, and possibly metabolic enzymes that are densely packed around myofibrils at triads. For the model to produce Ca^{2+} fluxes with peak values reported in the literature, the diffusiveness of Ca^{2+} across the barrier needs to increase by orders-of-magnitude as $[Ca^{2+}]_{js}$ rises. Movement in the cytosolic shells of RyRs when control hubs associated with A-sites become activated may alter interactions between RyRs with activated control hubs, activated DHPRs, and JPHs to increase the junctional gap between the SR and tubular membranes and change the properties of the barrier such as to allow Ca^{2+} to diffuse more freely from the JS into the rest of the cytosol. As suggested below, new experiments are needed to determine the nature of the barrier and characterize more fully its properties.

Suggested experiments to test the proposed hypothesis

Two types of experiments are suggested to test the foundations on which this hypothesis is based.

The diffusional JS/cytosol barrier in mammalian skeletal muscle should be further characterized preferably using Ca^{2+} probes targeted to the JS (Despa et al, 2014; Luo and Hill, 2014; Sanchez et al, 2021) under conditions where the magnitude of the steady RyR1 Ca^{2+} leak is altered by changing the SR Ca^{2+}-loading, altering $[Mg^{2+}]_c$, $[Ca^{2+}]_c$, or introducing modulators of RyR1 activity such as caffeine and low-level voltage-dependent activation of DHPRs. Alternatively, impermeant, low-affinity, negatively charged Ca^{2+}-dyes that diffuse very slowly across JS/cytosol barrier could be used with immobilized, freshly mechanically skinned muscle fibers with intact ECC (Lamb and Stephenson, 2018). The dye is first loaded for ∼30–60 min into the JS from a cytosolic solution containing the dye. The dye is then thoroughly washed out from the cytosol at large with several rinses. Changes in the dye signal predominantly from the JS upon rapid alteration of the Ca^{2+} leak could provide new information in support or against the presence of a selective diffusional barrier between the JS and the cytosol at large on which the hypothesis is based.

According to predictions based on the proposed hypothesis, there is a delay before a regenerative Ca^{2+} release spike occurs in the presence of 10 mM BAPTA (but not in the presence of 10 mM EGTA) after stimulation that causes DHPR activation when $[Ca^{2+}]_{SR} \leq 0.1$ mM. Measurements of SR Ca^{2+} release in mammalian muscle fibers, similar to those performed by Olivera and Pizarro (2018), under conditions that $[Ca^{2+}]_{SR} \leq 0.1$ mM at the time of stimulation in the presence of $[Ca^{2+}]_c < 10$ nM and critically that the ionic strength in the presence of 10 mM BAPTA is kept within the physiological range with K^+ as the main cation in solution can provide evidence in support or against the proposed hypothesis.

Appendix 1

Ion competition model for Mg^{2+} inhibition of RyR1s

The dual-inhibition model of RyR1 activity by Mg^{2+} in the presence of millimolar ATP specifies that RyR1s are inhibited when either Mg^{2+} is bound to cytosolic Ca^{2+} A-sites of the RyR1s or when cytosolic Ca^{2+}/Mg^{2+} I1-sites on the RyR1s are occupied by Ca^{2+} or Mg^{2+} (see reviews by Laver 2018; Meissner 2017; and references therein). Conversely, the RyR1s become maximally activated when the overall probability is highest for cytosolic

Ca^{2+} A-sites to be occupied by Ca^{2+} and the cytosolic Ca^{2+}/Mg^{2+} I1 sites are free of Ca^{2+} or Mg^{2+}.

The overall open probability (P_O) of a RyR1 channel is described as the product between an activation term P_{AO} and an inhibition term P_{IO}:

$$P_O = P_{AO} \times P_{IO} \quad \text{(A1)}$$

The activation term P_{AO} expresses the probability that the control hub of the RyR1 molecule containing the Ca^{2+} A-sites causes the RyR1 pore to open when Ca^{2+}/Mg^{2+} I1 sites on the RyR1 are not occupied by either Ca^{2+} or Mg^{2+}. On the other hand, the inhibition term P_{IO} expresses the probability that the pore of the RyR1 channel is not inhibited at the low-affinity Ca^{2+}/Mg^{2+} I1 sites.

Importantly, millimolar ATP activates RyR1s in the absence of Ca^{2+} ($[Ca^{2+}]$ = 1 nM) and Mg^{2+} (Smith et al., 1986; Meissner et al., 1986; Laver et al., 2004), and Mg^{2+} also potently inhibits RyR1 activation induced by ATP. These observations were quantitatively explained by reasoning that the pore of the RyR1 channel can open in the presence of millimolar ATP not only when Ca^{2+} is bound to the A-sites (as is the case in the absence of ATP) but also when the A-sites are free, or when two M_m^+ are bound to them (and inhibition at the Ca^{2+}/Mg^{2+} I1 sites is not complete) (Laver et al., 2004; see caption to Table II in Laver et al., 2004). P_i and P_{max} express the level of RyR1 activation (0 to 1) at the A-sites when the A-sites are free or have two M_m^+ bound to them, and when the A-sites are saturated with Ca^{2+}, respectively.

Ion competition at individual Ca^{2+} A-sites in the presence of ATP

All parameters associated with individual/protomeric ion binding sites on the RyR1 molecule are preceded by the "*1p*" superscript to distinguish them from corresponding parameters associated with activation of isolated RyR1 molecules that have four integrated protomers. The latter parameters are not preceded by a superscript.

Eq. A2 expresses the probability ${}^{1p}P_{AO}$ that an individual/protomeric A-site is activated in the presence of ATP by either Ca^{2+} being bound to it, by two M_m^+ such as K^+ (or Cs^+) being bound to it, or by being free at various cytosolic concentrations of Ca^{2+} ($[Ca^{2+}]_c$), Mg^{2+} ($[Mg^{2+}]_c$), and M_m^+ ($[M_m^+]_c$), when Ca^{2+}, Mg^{2+}, and M_m^+ compete for binding to the respective A-site. In contrast, the individual A-site is inhibited when Mg^{2+} is bound to it. The equilibrium dissociation constant of cytosolic Mg^{2+} from an individual A-site has the lowest value in the absence of luminal Ca^{2+} and increases when luminal $[Ca^{2+}]$ ($[Ca^{2+}]_L$) rises due to a non-competitive allosteric process (Laver et al., 2004) according to the following relation: ${}^{1p}K_{Mg}(1 + [Ca^{2+}]_L/{}^{1p}K_L)$, where ${}^{1p}K_{Mg}$ is the equilibrium dissociation constant of Mg^{2+} from the individual A-site in the absence of $[Ca^{2+}]_L$, and ${}^{1p}K_L$ is the Ca^{2+} dissociation constant from the luminal L-site of the respective protomer. ${}^{1p}P_i$ in Eq. A2 expresses the level of an individual A-site activation (0 to 1) in the absence of cytosolic Ca^{2+} and Mg^{2+}, when the A-site is free, or has two M_m^+ bound to it, while ${}^{1p}P_{max}$ expresses the level of activation at the A-site in the presence of millimolar ATP at saturating $[Ca^{2+}]_c$. $[{}^{1p}K_{Mm}]^2$ is the dissociation constant of two M_m^+ from the A-site considering that a divalent cationic site is likely to bind two M_m^+ and ${}^{1p}K_{CaA}$ is the Ca^{2+} dissociation constant from the A-site. At steady state,

$${}^{1p}P_{AO} = \frac{\left({}^{1p}P_i\left(1 + \frac{[M_m^+]_c^2}{({}^{1p}K_{Mm})^2}\right) + {}^{1p}P_{max}\frac{[Ca^{2+}]_c}{{}^{1p}K_{CaA}}\right)}{1 + \frac{[M_m^+]_c^2}{({}^{1p}K_{Mm})^2} + \frac{[Ca^{2+}]_c}{{}^{1p}K_{CaA}} + \frac{[Mg^{2+}]_c}{{}^{1p}K_{Mg}\left(1 + \frac{[Ca^{2+}]_L}{{}^{1p}K_L}\right)}} \quad \text{(A2)}$$

Activation of isolated RyR1 molecules at Ca^{2+} A-sites in the presence of millimolar ATP

Since the control hub of one RyR1 molecule includes the A- and L-sites of all four protomers, activation of the RyR1 hub would require that all four protomers have their A-site activated. In this scenario, the activation term P_{AO} in Eq. A1 expresses the probability that all four protomers on a RyR1 molecule have their A-site activated. Then, if each protomer is independently activated at its A-site with probability ${}^{1p}P_{AO}$, the probability that all four protomers are activated is given by $({}^{1p}P_{AO})^4$, and P_{AO} is given by Eq. A3:

$$P_{AO} = (P_{AO1p})^4 \quad \text{(A3)}$$

Conversely, if the value of the activation term P_{AO} is known at the level of one RyR1 molecule, then the probability ${}^{1p}P_{AO}$ of an individual RyR1 protomer to have its A-site activated in the presence of millimolar ATP, is given by Eq. A4

$$P_{AO1p} = (P_{AO})^{0.25} \quad \text{(A4)}$$

Based on the experimental results of Laver et al. (2004) on the open probability of isolated RyR1s incorporated in lipid bilayers in the presence of 2 mM ATP and Eqs. A2, A3, and A4, one can derive all parameter values necessary to quantitatively describe activation at individual A-sites under different ionic conditions with respect to luminal Ca^{2+} and cytosolic Ca^{2+}, Mg^{2+}, and M_m^+ concentrations, and quantitatively verify how well predictions based on Eqs. A2 and A3 can explain experimental observations made on isolated RyR1s.

Derivation of parameter values for activation at individual Ca^{2+} A-sites of RyR1 in the presence of millimolar ATP

Derivation of ${}^{1p}P_{max}$ and ${}^{1p}P_i$ parameter values

The value of ${}^{1p}P_{max}$ can be derived from the maximum RyR1 open probability, P_{Max}, when $[Ca^{2+}]_c$ is raised in the absence of Mg^{2+} using Eq. A2. According to Table I of Laver et al. (2004), P_{Max} = 0.86 at both 0.01 and 1 mM $[Ca^{2+}]_L$. Substituting P_{AO} with P_{Max} and ${}^{1p}P_{PO}$ with ${}^{1p}P_{max}$ in Eq. A4, it follows that ${}^{1p}P_{max}$ = 0.963 and is independent of $[Ca^{2+}]_L$ in the range 0.01–1 mM.

${}^{1p}P_i$ refers to the level of individual A-site activation in the absence of cytosolic Ca^{2+} and Mg^{2+}. According to Eq. A2 ${}^{1p}P_{AO}$ = ${}^{1p}P_i$ in the absence of cytosolic Ca^{2+} ($[Ca^{2+}]_c \leq 1$ nM) and Mg^{2+}. Similarly, P_i refers to the level of individual A-site activation in the absence of cytosolic Ca^{2+} and Mg^{2+}, hence $P_{AO} = P_i$. Moreover, since all Ca^{2+}/Mg^{2+} I1 sites on the RyR1 molecule are free in the

absence of cytosolic Ca^{2+} and Mg^{2+}, and therefore, $P_{I0} = 1$, it follows from Eq. A1 that $P_O = P_{AO}$ $(= P_i)$. Furthermore, since ${}^{1p}P_{AO} = (P_{AO})^{0.25}$ in Eq. A4, it means that ${}^{1p}P_i = {}^{1p}P_{AO} = (P_{AO})^{0.25} = (P_O)^{0.25}$ in the absence of cytosolic Ca^{2+} and Mg^{2+}. Laver et al. (2004) reported P_O values of 0.21 ± 0.16 and 0.25 ± 0.07 for RyR1s in the presence of 50 and 250 mM cytosolic $[Cs^+]$, respectively, when $[Ca^{2+}]_L$ = 0.1 mM, $[Ca^{2+}]_c$ = 1 nM, and $[Mg^{2+}]_c$ = 0 (Table III in Laver et al. (2004), Control column). Since the mean P_O values are close to each other and not statistically significantly different from each other, it indicates that P_O is not sensitive to $[M_m{}^+]_c$ in the range 50–250 mM in the absence of cytosolic Ca^{2+} and Mg^{2+}. Using the mean average value for P_O = 0.23 in the absence of cytosolic Ca^{2+} and Mg^{2+} when $[Ca^{2+}]_L$ = 0.1 mM, it follows that ${}^{1p}P_i \approx (0.23)^{0.25} = 0.6925$. Similarly, the values reported by Laver et al. (2004) in Table III for P_O at $[Ca^{2+}]_L$ = 1 mM in 50 mM (0.45 ± 0.20) and 250 mM (0.58 ± 0.06) cytosolic $[Cs^+]$ in the absence of cytosolic Ca^{2+} and Mg^{2+} are relatively close and not statistically significantly different from each other, supporting the view that P_i is not sensitive to $[M_m{}^+]_c$ in the range 50–250 mM in the absence of cytosolic Ca^{2+} and Mg^{2+}. Taking the mean average value of 0.515 for P_O in the absence of cytosolic Ca^{2+} and Mg^{2+} when $[Ca^{2+}]_L$ = 1 mM, it follows that ${}^{1p}P_i \approx (0.515)^{0.25} = 0.8471$.

When $[Ca^{2+}]_L$ was raised to 3 mM in the absence of cytosolic Ca^{2+} ($[Ca^{2+}]_c$ = 1 nM) and Mg^{2+} in 250 mM cytosolic $[Cs^+]$, Laver et al. (2004) reported in Table III a P_O value of 0.63 ± 0.07. Using the same approach, the derived value for ${}^{1p}P_i$ $(= (P_O)^{0.25})$ is 0.891 when $[Ca^{2+}]_L$ = 3 mM. Laver et al. (2004) also reported in Table I that P_i = 0.1 ± 0.07 in 250 mM $[Cs^+]$ when $[Ca^{2+}]_L$ was 0.01 mM. The derived value for ${}^{1p}P_i$ $(= (P_i)^{0.25})$ based on Eq. A4 is 0.562. Thus, P_i is sensitive to $[Ca^{2+}]_L$ but not to the cytosolic $[M_m{}^+]$ in the range 50–250 mM.

The dependence of ${}^{1p}P_i$ on $[Ca^{2+}]_L$ over the $[Ca^{2+}]_L$ range 0.01–3 mM is well predicted by Eq. A5 (0.573 versus 0.562 at 0.01 mM $[Ca^{2+}]_L$; 0.66 versus 0.692 at 0.1 mM $[Ca^{2+}]_L$; 0.84 at 1 mM $[Ca^{2+}]_L$ and 0.883 at 3 mM $[Ca^{2+}]_L$):

$$ {}^{1p}P_i([Ca^{2+}]_L) = 0.56 + \frac{0.35}{1 + \frac{0.25\text{mM}}{[Ca^{2+}]_L}} \tag{A5} $$

Derivation of ${}^{1p}K_{Mm}{}^2$, ${}^{1p}K_L$, and ${}^{1p}K_{Mg}$ parameter values

In the absence of $[Ca^{2+}]_c$, Eq. A2 reduces to Eq. A6:

$$ {}^{1p}P_{AO} = \frac{{}^{1p}P_i\left(1 + \frac{[M_m^+]_c^2}{({}^{1p}K_{Mm})^2}\right)}{1 + \frac{[M_m^+]_c^2}{({}^{1p}K_{Mm})^2} + \frac{[Mg^{2+}]_c}{{}^{1p}K_{Mg}\left(1 + \frac{[Ca^{2+}]_L}{{}^{1p}K_L}\right)}} $$

or

$$ \left(\frac{{}^{1p}P_i}{{}^{1p}P_{AO}} - 1\right){}^{1p}K_{Mg}\left(1 + \frac{[Ca^{2+}]_L}{{}^{1p}K_L}\right) = \frac{[Mg^{2+}]_c}{1 + \frac{[M_m^+]_c^2}{({}^{1p}K_{Mm})^2}} \tag{A6} $$

According to Table III in Laver et al. (2004), the P_O values measured at $[Ca^{2+}]_L$ = 0.1 mM in the absence of Ca^{2+} ($[Ca^{2+}]_c$ = 1 nM) and Mg^{2+} were reduced 50% by 8 μM cytosolic $[Mg^{2+}]_c$ in the presence of $[Cs^+]_c$ = 50 mM and by 20 μM $[Mg^{2+}]_c$ in the presence of $[Cs^+]_c$ = 250 mM. Since inhibition at the Ca^{2+}/Mg^{2+}-I1 sites is negligible (<0.7%) at these low $[Mg^{2+}]_c$ in the absence of cytosolic Ca^{2+}, it follows that $P_O = P_{AO}$ in the absence of $[Ca^{2+}]_c$ and $[Mg^{2+}]_c$ and $P_O \approx P_{AO}$ when $[Mg^{2+}]_c \le 8$ μM at 50 mM and ≤20 μM at 250 mM $[M_m{}^+]_c$. Consequently, ${}^{1p}P_{AO}$ = 0.6925 when $P_O = P_{AO}$ = 0.23 and is not sensitive to $[M_m{}^+]_c$ in the range 50–250 mM in the absence of $[Ca^{2+}]_c$ and $[Mg^{2+}]_c$. The 50% reduction of P_O from 0.23 to 0.115 corresponds to the reduction of ${}^{1p}P_{AO}$ from 0.695 to ≈ 0.582 $(= (0.115)^{0.25})$ based on Eq. A4. ${}^{1p}P_i$ is also insensitive to the $[M_m{}^+]_c$ in the range 50–250 mM at constant $[Ca^{2+}]_L$ since by definition ${}^{1p}P_i = {}^{1p}P_{AO}$ in the absence of Ca^{2+} and Mg^{2+}. The value of the left term in Eq. A6 $({}^{1p}P_i/{}^{1p}P_{AO} - 1)$ $({}^{1p}K_{Mg}(1 + [Ca^{2+}]_L/{}^{1p}K_L))$ is therefore the same at 50 and 250 mM $[M_m{}^+]_c$ for conditions where ${}^{1p}P_{AO}$ is reduced to 0.582 at 0.1 mM $[Ca^{2+}]_L$. The rightside term in Eq. A6 $([Mg^{2+}]_c/(1 + [M_m{}^+]_c{}^2/{}^{1p}K_{Mm}{}^2)$ must have the same value when P_{AO} (0.23) decreases by the same fraction (50%) in 50 and 250 mM $[Cs^+]_c$, i.e., 8 μM/(1 + 2,500 $mM^2/{}^{1p}K_{Mm}{}^2$) = 20 μM/(1 + 62,500 $mM^2/{}^{1p}K_{Mm}{}^2$). Consequently, ${}^{1p}K_{Mm}{}^2$ = 37,500 mM^2, ${}^{1p}K_{Mm}$ = 193.6 mM, and the value of the right side term of Eq. A6 is 7.5 μM (8 μM/1.06(6) = 20 μM/(2.6(6)), meaning that $({}^{1p}P_i/{}^{1p}P_{AO} - 1)$ $({}^{1p}K_{Mg}(1 + [Ca^{2+}]_L/{}^{1p}K_L)) = 7.5$ μM. Since $({}^{1p}P_i/{}^{1p}P_{AO} - 1) = (0.6925/0.582 - 1) = 0.18986$ and $[Ca^{2+}]_L$ = 0.1 mM, it follows that ${}^{1p}K_{Mg}(1 + 0.1\,mM/{}^{1p}K_L) = 39.5$ μM.

${}^{1p}K_{Mm}{}^2$ can also be evaluated from the P_O measurements of Laver et al. (2004) in Table III for 1 mM $[Ca^{2+}]_L$ at 50 and 250 mM $[Cs^+]_c$. The values of P_O measurements made at 1 mM $[Ca^{2+}]_L$ for 50 and 250 mM $[Cs^+]_c$ in the absence of Ca^{2+} and Mg^{2+} were similar and not statistically significantly different from each other, indicating that P_O is not sensitive to $[M_m{}^+]_c$ in the range 50–250 mM. Consequently, the mean value of the two sets of measurements (P_O = 0.515) was taken to describe the open RyR1 probability in the absence of Ca^{2+} and Mg^{2+} at 1 mM $[Ca^{2+}]_L$. Since in this case there is no inhibition at the I1 sites, $P_{AO} = P_O$ = 0.515 and ${}^{1p}P_i = {}^{1p}P_{AO} = (0.515)^{0.25} = 0.8471$. The value of P_O was reduced by 50% in the presence of 20 μM $[Mg^{2+}]_c$ in the 50 mM $[Cs^+]_c$ solution and 72 μM $[Mg^{2+}]_c$ in the 250 mM $[Cs^+]_c$ solution in the absence of cytosolic Ca^{2+} ($[Ca^{2+}]_c \le 1$ nM) when $[Ca^{2+}]_L$ was kept at 1 mM. Note that inhibition at the I1 sites was estimated to be ∼4% in the presence of 20 μM $[Mg^{2+}]_c$ at 50 mM $[Cs^+]_c$ and negligible (<0.1%) in the presence of 72 μM $[Mg^{2+}]_c$ at 250 mM $[Cs^+]_c$. In view of this, $P_O = P_{AO} = (0.515/2)$ and ${}^{1p}P_{AO} = (0.515/2)^{0.25} = 0.712$ for 250 mM $[Cs^+]_c$, and $P_{AO} = 0.2678$ $(= 1.04 \times 0.515/2)$ and ${}^{1p}P_{AO} = (0.2678)^{0.25} = 0.719$. Dividing the left side term of Eq. A6 for 50 mM $[Cs^+]_c$ by the left side term of Eq. A6 for 250 mM $[Cs^+]_c$ and the right side term of Eq. A6 for 50 mM $[Cs^+]_c$ by the right side term of Eq. A6 for 250 mM $[Cs^+]_c$, one obtains the following expression: (0.8471/0.719 – 1)/(0.8471/0.712 – 1) = (20 μM/72 μM)(1 + 62,500/${}^{1p}K_{Mm}{}^2$)/(1 + 2,500 $mM^2/{}^{1p}K_{Mm}{}^2$) or 3.384 (1 + 2,500 $mM^2/{}^{1p}K_{Mm}{}^2$) = (1 + 62,500 $mM^2/{}^{1p}K_{Mm}{}^2$) and ${}^{1p}K_{Mm}{}^2$ = 22,668 mM^2 with ${}^{1p}K_{Mm}$ = 150.6 mM. Furthermore, from Eq. A6, it follows that ${}^{1p}K_{Mg}(1 + 1\,mM/{}^{1p}K_L) = ([Mg^{2+}]_c/(1 + [M_m{}^+]_c{}^2/{}^{1p}K_{Mm}{}^2))$ $({}^{1p}P_{AO}/({}^{1p}P_i - {}^{1p}P_{AO}))$ = 119.1 μM.

The ${}^{1p}K_L$ and $[Mg^{2+}]_c$ values were obtained by solving the system of equations: ${}^{1p}K_{Mg}(1 + 0.1\,mM/{}^{1p}K_L) = 39.5$ μM and ${}^{1p}K_{Mg}(1 + 1\,mM/{}^{1p}K_L) = 119.1$ μM, which yielded ${}^{1p}K_L$ = 346.6 μM and ${}^{1p}K_{Mg}$ = 30.65 μM.

The values for ${}^{1p}K_{Mm}$ obtained from the two sets of independent measurements were 193.6 and 150.6 mM. The mean value for ${}^{1p}K_{Mm}$ obtained from the two sets of measurements (172.1 mM) was used for quantitative predictions of RyR1 activation.

Derivation of ${}^{1p}K_{CaA}$ parameter value

Laver et al. (2004) used Eq. A7 to describe the relation between P_{A0} and $[Ca^{2+}]_c$ in the absence of $[Mg^{2+}]_c$, where K_a is the $[Ca^{2+}]_c$ value at half-activation ($[Ca^{2+}]_c^{50}$):

$$P_{A0} = P_i + (P_{Max} - P_i)/(1 + K_a/[Ca^{2+}]_c) \quad \text{(A7)}$$

In the absence of $[Mg^{2+}]_c$, the relation between P_{A0} and $[Ca^{2+}]_c$ is described by Eq. A8, which is derived from Eqs. A2 and A3:

$$P_{A0} = ({}^{1p}P_{A0})^4 = \left(\frac{\left({}^{1p}P_i \left(1 + \frac{[M_m^+]_c^2}{({}^{1p}K_{Mm})^2} \right) + {}^{1p}P_{max} \frac{[Ca^{2+}]_c}{{}^{1p}K_{CaA}} \right)}{1 + \frac{[M_m^+]_c^2}{({}^{1p}K_{Mm})^2} + \frac{[Ca^{2+}]_c}{{}^{1p}K_{CaA}}} \right)^4 \quad \text{(A8)}$$

Since $P_i = ({}^{1p}P_i)^4$ and $P_{Max} = ({}^{1p}P_{max})^4$, it follows that the minimum (P_i) and the maximum (P_{Max}) values of the P_{A0} curves generated by Eq. A7 are the same as the minimum $({}^{1p}P_i)^4$ and the maximum $({}^{1p}P_{max})^4$ values of the P_{A0} curves generated by Eq. A8.

According to Eq. A7, half-activation $P_{50} = (P_i + P_{Max})/2$ happens when $[Ca^{2+}]_c = K_a$. The value of ${}^{1p}K_{CaA}$ can then be calculated from Eq. A8 after substitution of P_{A0} with $(P_i + P_{Max})/2$ and $[Ca^{2+}]_c$ with K_a. The value of K_a at 0.01 mM $[Ca^{2+}]_L$ (0.4 ± 0.1 µM) is not significantly different from that at 1 mM $[Ca^{2+}]_L$ (0.3 ± 0.1 µM) according to Table I and Fig. 1 of Laver et al. (2004). Therefore, K_a is considered to have the intermediary value of 0.35 µM and be independent of $[Ca^{2+}]_L$ in the range 0.01–1 mM.

From Table I of Laver et al. (2004), $P_i = 0.4$ and $P_{Max} = 0.86$ at $[Ca^{2+}]_L$ = 1 mM, $[Cs^+]_c$ = 250 and 2 mM ATP such that P_{A0} at half-activation point, $P_{50} = (P_i + P_{Max})/2 = 0.63$. Based on this information, the relevant parameters in Eq. A8 have the following values: $P_{A0} = 0.63$, ${}^{1p}P_i = (0.4)^{0.25} = 0.795$, ${}^{1p}P_{max} = (0.86)^{0.25} = 0.963$, $[Ca^{2+}]_c = 0.35$ µM, $1 + [M_m^+]_c^2/{}^{1p}K_{Mm}^2 = 1 + (250/172.1)^2 = 3.1$ (using estimated ${}^{1p}K_{Mm}$ value of 172.1 mM as described above). Substituting the values of these parameters in Eq. A8, it follows that $0.63 = \{[(0.795 \times 3.1 + 0.963 \times 0.35\ \mu M/{}^{1p}K_{CaA})/(3.1 + 0.35\ \mu M/{}^{1p}K_{CaA})]\}^4$ and ${}^{1p}K_{CaA} = 0.085$ µM = 85 nM.

Another estimate for ${}^{1p}K_{CaA}$ is obtained from measurements reported by Laver et al. (2004) in Table I at $[Ca^{2+}]_L$ = 0.01 mM, $[Cs^+]_c$ = 250 mM, 2 mM ATP, $P_i = 0.1$, $P_{Max} = 0.86$. The values of the relevant parameters in Eq. A8 are: $P_{A0} = (P_i + P_{Max})/2 = 0.48$, ${}^{1p}P_i = (0.1)^{0.25} = 0.5623$, ${}^{1p}P_{max} = (0.86)^{0.25} = 0.963$, $[Ca^{2+}]_c = 0.35$ µM, $1 + [M_m^+]_c^2/{}^{1p}K_{Mm}^2 = 1 + (250/172.1)^2 = 3.1$. Substitution of parameters in Eq. A8 with their values leads to the following expression: $0.48 = [(0.5623 \times 3.1 + 0.963 \times 0.35\ \mu M/{}^{1p}K_{CaA})/(3.1 + 0.35\ \mu M/{}^{1p}K_{CaA})]^4$ and ${}^{1p}K_{CaA} = 0.0546$ µM = 54.6 nM.

Based on these two estimates (85 and 54.6 nM), the dissociation constant of Ca^{2+} from the Ca^{2+} A-site of a RyR1 protomer, ${}^{1p}K_{CaA}$, is approximated to 70 nM.

The values of parameters ${}^{1p}P_i$, ${}^{1p}K_{Mm}{}^2$, ${}^{1p}P_{max}$, ${}^{1p}K_{CaA}$, ${}^{1p}K_{Mg}$, and ${}^{1p}K_L$ derived in the Appendix needed to quantitatively describe P_{A0} under different ionic conditions are shown in Table 1.

How predictions based on Eqs. A3 and A4 compare with predictions derived from generic Hill equations

Laver et al. (2004) used to fit the data points for the activation section of the open probability of isolated RyR1s incorporated in lipid bilayers (P_{A0}) in the presence of 2 mM ATP using curves generated by generic Hill Equations such as Eq. A7.

Fig. A1 displays pairs of curves generated by Eqs. A7 and A8 that have the same minima and maxima and have the mid $P_0{}^{50}$ [$= (P_i + P_{Max})/2$] occurring at the same $[Ca^{2+}]_c$. For this to happen, ${}^{1p}P_i = (P_i)^{0.25}$, ${}^{1p}P_{max} = (P_{Max})^{0.25}$, and

$${}^{1p}K_{CaA} = \frac{K_a \left({}^{1p}P_{max} - (P_0^{50})^{0.25} \right)}{\left(1 + \frac{[M_m^+]_c^2}{({}^{1p}K_{Mm})^2} \right) (P_0^{50})^{0.25} - {}^{1p}P_i)} \quad \text{(A9)}$$

As shown in Fig. A1, the two curves generated by Eqs. A7 and A8 when $[Ca^{2+}]_L$ = 1 mM effectively overlap over the entire $[Ca^{2+}]_c$ range while the two curves when $[Ca^{2+}]_L$ = 0.01 mM are equally suitable for fitting experimental data. Importantly, the qualitative distinguishing feature between the two curves in a pair is that the curves generated by Eq. A8 are based on the knowledge that there is one Ca^{2+} A-site for each of the four protomers that constitute the RyR1 molecule, while the curves generated by Eq. A7 are based on the presumption that there is only one Ca^{2+} A-site per RyR1 molecule.

Eq. A10, derived from Eqs. A2 and A3, in conjunction with parameter values in Table 1 describe activation at the Ca^{2+} A-sites of isolated RyR1s in the presence of mM ATP and different ionic conditions with respect to $[Ca^{2+}]_c$, $[Mg^{2+}]_c$, $[M_m^+]_c$, and $[Ca^{2+}]_L$

$$P_{A0} = (P_{A0\,1p})^4 = \left(\frac{\left({}^{1p}P_i \left(1 + \frac{[M_m^+]_c^2}{({}^{1p}K_{Mm})^2} \right) + {}^{1p}P_{max} \frac{[Ca^{2+}]_c}{{}^{1p}K_{CaA}} \right)}{1 + \frac{[M_m^+]_c^2}{({}^{1p}K_{Mm})^2} + \frac{[Ca^{2+}]_c}{{}^{1p}K_{CaA}} + \frac{[Mg^{2+}]_c}{{}^{1p}K_{Mg} \left(1 + \frac{[Ca^{2+}]_L}{{}^{1p}K_L} \right)}} \right)^4 \quad \text{(A10)}$$

Ion inhibition at the RyR1 Ca^{2+}/Mg^{2+}-I1 sites

The inhibition term P_{I0} expresses the probability that the pore of the RyR1 channel is not inhibited at the low-affinity Ca^{2+}/Mg^{2+}-I1 sites in the presence of Mg^{2+} and Ca^{2+} ions that can bind to the Ca^{2+}/Mg^{2+}-I1 sites on the RyR1 molecule.

Since Ca^{2+}/Mg^{2+}-I1 sites on individual RyR1s appear to have the same affinity for Ca^{2+} and Mg^{2+} (Laver et al., 2004), P_{I0} depends on the sum of $[Ca^{2+}]_c + [Mg^{2+}]_c = [CaMg]_c$, rather than on

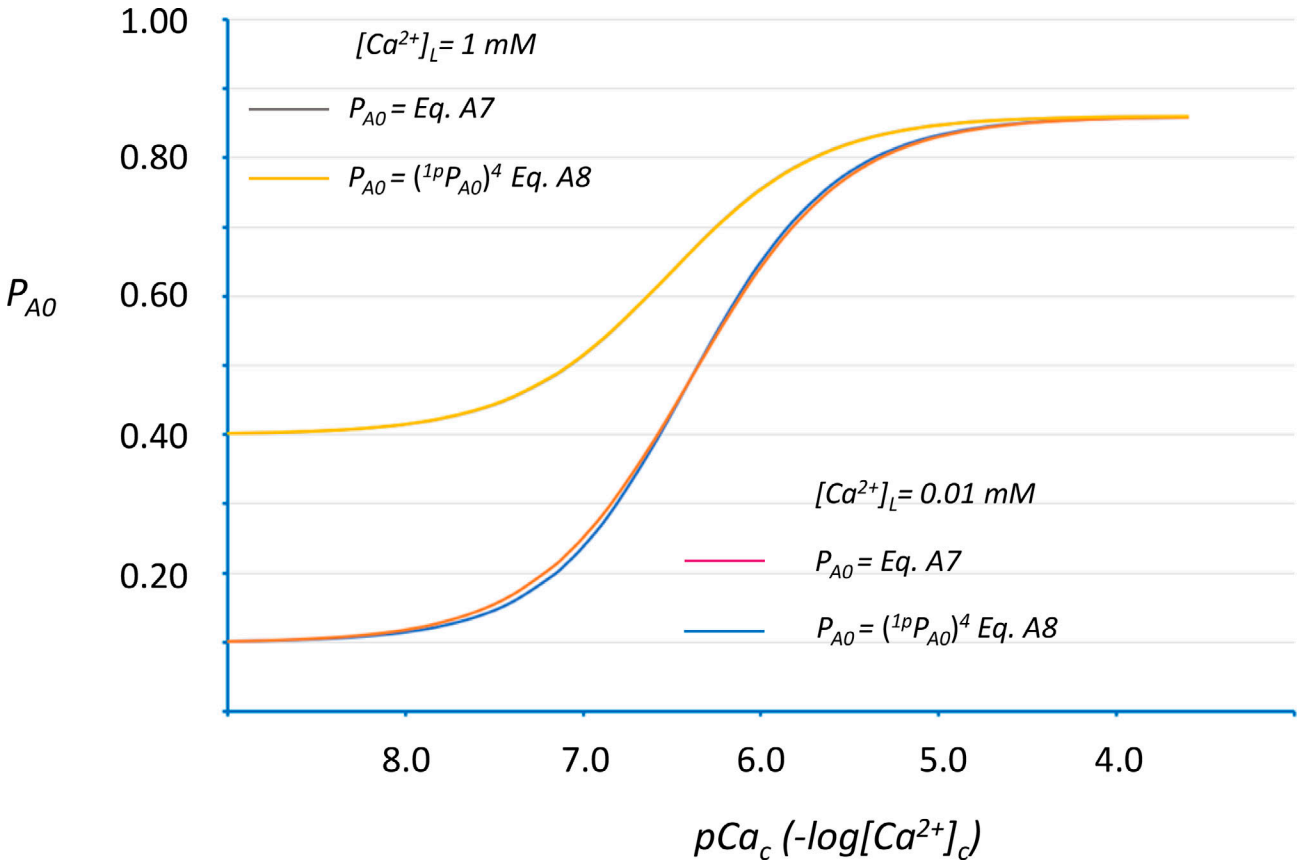

Figure A1. **Comparison between generic curves used to fit empirical data for P_{A0} dependence on $[Ca^{2+}]_c$ in isolated RyR1 with curves constructed based on a model that incorporates observations on functional and structural features of RyR1s.** The generic curves P_{A0} versus $[Ca^{2+}]_c$ produced by Eq. A7 used to fit experimental data on isolated RyR1s incorporated in lipid bilayers for $[Ca^{2+}]_L$ = 0.01 and 1 mM (Laver et al., 2004) are characterized by three parameters P_i, P_{Max}, and K_a, which represents $[Ca^{2+}]_c$ at half-activation $[(P_i + P_{Max})/2]$. These curves are compared with equivalent P_{A0} versus $[Ca^{2+}]_c$ curves generated by Eq. 8, which was derived based on a model where the control hub of one RyR1 molecule becomes activated when all four A-sites of the RyR1 molecule are independently activated. Experimental data can be equally well fit by generic and model-derived curves when the curves are forced to have the same minima, maxima, and intersect at their half-activation point. The $^{1p}K_{CaA}$ values derived from Eq. 9 to ensure that the model-generated curve intersects the generic curve at the mid point were 62.2 and 72.7 nM for $[Ca^{2+}]_L$ = 0.01 and 1 mM, respectively, in line with the $^{1p}K_{CaA}$ value of 70 nM in Table 1.

specific $[Ca^{2+}]_c$ and $[Mg^{2+}]_c$. K_{in} in Eq. A11 corresponds to the $[CaMg]_c$ at which RyR1s display 50% inhibition at the Ca^{2+}/Mg^{2+}-I1 sites. The second power of the term $[CaMg]_c^2/K_{in}^2$ in the Hill Eq. A11 was experimentally determined when the Mg^{2+} inhibition at the Ca^{2+}/Mg^{2+}-I1 sites was measured in single RyR1 channels (Laver et al., 1997a, 1997b, 2004):

$$P_{I0} = \frac{1}{1 + \frac{[CaMg]_c^2}{K_{in}^2}} \quad \text{(A11)}$$

As mentioned elsewhere, the Ca^{2+}/Mg^{2+}-I1 sites on RyR1s are particularly sensitive to ionic strength and other factors that do not affect the Ca^{2+} A-sites (Shomer et al., 1993; Meissner et al., 1997; Laver et al., 1997a, 1997b, 2004), suggesting that the strength of Mg^{2+} (and Ca^{2+}) binding to these low-affinity sites can be readily altered by subtle changes in the arrangement of negative charges that demarcate these sites. For example, the decrease in ionic strength by 150 mM associated with the reduction of $[Cs^+]_c$ from 250 to 100 mM caused a 10-fold reduction in $[Ca^{2+}]_c$ for 50% inhibition at the low-affinity Ca^{2+}/Mg^{2+}-I1 sites on RyR1s (Laver et al., 2004; Table I). As justified in the text, 50% inhibition at the Ca^{2+}/Mg^{2+}-I1 sites of RyR1s is likely to occur at ≈50 µM Mg^{2+} based on measurements of Ca^{2+} release from native triads made by Donoso et al. (2000).

For skeletal muscle fibers at rest, Eq. A12, where K_{in} = 0.05 mM, is taken to describe the probability $^{nc}P_{I0}$ that the gates of $^{nc}RyR1s$ are not blocked from opening by Ca^{2+}/Mg^{2+} occupation at the I1-sites:

$$^{nc}P_{I0} = \frac{1}{1 + \frac{([CaMg]_{js})^2}{K_{in}^2}} \quad \text{(A12)}$$

Evidence that DHPRs can exert an additional inhibitory action on $^{c}RyR1s$ in mammalian skeletal muscle fibers (see Kirsch et al., 2001; Zhou et al., 2006; and references therein) can be accommodated by assuming that DHPRs increase the level of cooperativity for Ca^{2+}/Mg^{2+} binding to the I1 sites of $^{c}RyR1s$ Ca^{2+}/Mg^{2+} while displaying 50% inhibition at same $[CaMg]_{js}$ (0.05 mM) as $^{nc}RyR1s$. For example, if the four Ca^{2+}/Mg^{2+} inhibitory I1 sites on a $^{c}RyR1$ molecule act cooperatively to cause quasi-simultaneous binding and dissociation of four Ca^{2+}/Mg^{2+} ions by a two-state allosteric mechanism that is akin to the binding of four O_2 to one

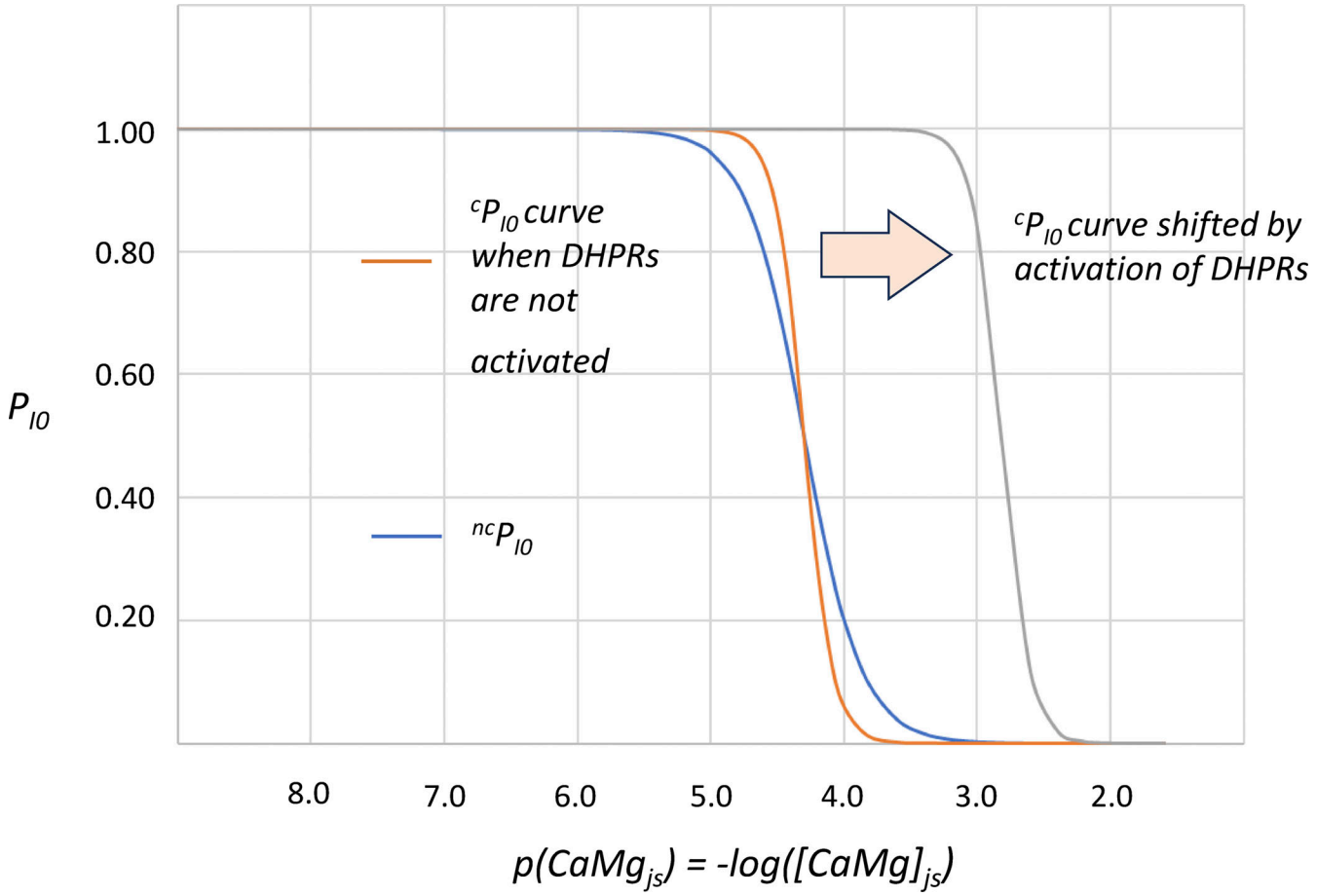

Figure A2. **Semilogarithmic plot of $^{nc}P_{I0}$ and $^{c}P_{I0}$ dependence on the combined concentrations of Ca^{2+} and Mg^{2+} in the junctional space ($[CaMg]_{js}$).** The inhibition terms $^{nc}P_{I0}$ and $^{c}P_{I0}$ express the probabilities that ^{nc}*RyR1s* and, respectively, ^{c}*RyR1s* are not inhibited at the low affinity Ca^{2+}/Mg^{2+} I1 sites. Under resting conditions, when the DHPRs are not activated, both terms display 50% inhibition at 50 µM $[CaMg]_{js}$ but the increased DHPR-dependent level of cooperativity between the four I1 sites of ^{c}*RyR1s* translates to greater inhibition at $[CaMg]_{js}$ > 50 µM in ^{c}*RyR1s* than ^{nc}*RyR1s*. A 30-fold rise of $^{4p}K_{in}$ induced by DHPR activation would shift the $^{c}P_{I0}$ curve to the right, triggering rapid Ca^{2+} release from SR (see Fig. 1 and text).

hemoglobin molecule consisting of four subunits (Viappiani et al., 2014), then the ^{c}*RyR1* channel is blocked from opening at the Ca^{2+}/Mg^{2+} inhibitory I1 sites when all four I1-inhibitory sites are occupied, and the channel is allowed to open when all four I1-inhibitory sites are free. The probability $^{c}P_{I0}$ that ^{c}*RyR1* channels are not blocked from opening at their inhibitory I1 sites at given $[CaMg]_{js}$ is then described by Eq. A13 with $^{4p}K_{in}$ = 0.05 mM:

$$^{c}P_{I0} = \frac{1}{1 + \frac{\left([CaMg]_{js}\right)^{4}}{\left(^{4p}K_{in}\right)^{4}}} \quad \text{(A13)}$$

Fig. A2 shows the $^{c}P_{I0}$ dependence on $[CaMg]_{js}$ based on Eq. A13 in comparison with the dependence of $^{nc}P_{I0}$ on $[CaMg]_{js}$ using Eq. A12. The two curves intersect at their mid-point where $[CaMg]_{js}$ = 0.05 mM. The steeper decline of $^{c}P_{I0}$ compared with $^{nc}P_{I0}$ indicates that inhibition at the Ca^{2+}/Mg^{2+}-I1 sites is more complete for ^{c}*RyR1s* than for ^{nc}*RyR1s* at $[CaMg]_{js}$ >0.05 mM. For example, under physiological conditions, when $[Mg^{2+}]_{c} \approx [Mg^{2+}]_{js}$ = 1 mM, ^{c}*RyR1s* would be inhibited 99.99 % at the Ca^{2+}/Mg^{2+}-I1 sites ($^{c}P_{I0}$ = 0.01%) in the presence of 0.1 µM $[Ca^{2+}]_{js}$ compared with the ^{nc}*RyR1s* that would be only 99% inhibited ($^{nc}P_{I0}$ = 1%). This means that the number of ^{nc}*RyR1s* that can become activated at 1 mM $[Mg^{2+}]_{js}$ and 0.1 µM $[Ca^{2+}]_{js}$ is 100-fold greater than the number of ^{c}RyR1s. Thus, stronger cooperativity for Ca^{2+}/Mg^{2+} binding at the Ca^{2+}/Mg^{2+} inhibitory sites on ^{c}RyR1s would considerably increase the level of RyR1 inhibition in a muscle fiber at rest. The increased inhibitory effect exerted by DHPRs on RyR1s in mammalian skeletal muscle can largely explain why interventions that prevent or disrupt interactions between DHPRs and the RyR1s reduce the stability of junctional RyR1 arrays and increase the occurrence of spontaneous spark-like events (Shirokova et al., 1999; Kirsch et al., 2001; Zhou et al., 2006).

Quantification of the open probability of RyR1s in skeletal muscle

Based on Eqs. A10, A12, and A13, and parameter values in Table 1, one can now evaluate the dependence of the open probability of ^{nc}*RyR1s* ($^{nc}P_{O}$) and ^{c}*RyR1s* ($^{c}P_{O}$) at steady state, on $[Ca^{2+}]_{SR}$ and ionic composition of the JS to which the cytosolic regulatory A- and I1 sites of RyR1s are exposed:

$$ {}^{nc}P_0 = P_{A0} \times {}^{nc}P_{I0} = \frac{\left({}^{1p}P_i\left(1+\frac{[M_m]_{js}^2}{({}^{1p}K_{Mm})^2}\right)+{}^{1p}P_{max}\frac{[Ca^{2+}]_{js}}{{}^{1p}K_{CaA}}\right)^4}{\left(1+\frac{[M_m]_{js}^2}{({}^{1p}K_{Mm})^2}+\frac{[Ca^{2+}]_{js}}{{}^{1p}K_{CaA}}+\frac{[Mg^{2+}]_{js}}{{}^{1p}K_{Mg}\left(1+\frac{[Ca^{2+}]_{SR}}{{}^{1p}K_L}\right)}\right)^4} \times \frac{1}{1+\left(\frac{[CaMg]_{js}}{K_{in}}\right)^2} \quad \text{(A14)} $$

$$ {}^{c}P_0 = P_{A0} \times {}^{c}P_{I0} = \frac{\left({}^{1p}P_i\left(1+\frac{[M_m]_{js}^2}{({}^{1p}K_{Mm})^2}\right)+{}^{1p}P_{max}\frac{[Ca^{2+}]_{js}}{{}^{1p}K_{CaA}}\right)^4}{\left(1+\frac{[M_m]_{js}^2}{({}^{1p}K_{Mm})^2}+\frac{[Ca^{2+}]_{js}}{{}^{1p}K_{CaA}}+\frac{[Mg^{2+}]_{js}}{{}^{1p}K_{Mg}\left(1+\frac{[Ca^{2+}]_{SR}}{{}^{1p}K_L}\right)}\right)^4} \times \frac{1}{1+\left(\frac{[CaMg]_{js}}{{}^{4p}K_{in}}\right)^4} \quad \text{(A15)} $$

However, during rapid changes in $[Ca^{2+}]_{js}$ when the regulatory sites on the RyR1s are not at steady state with the ions in their environment, ${}^{nc}P_0$ and ${}^{c}P_0$ are time-sensitive (${}^{nc}P_0\ (t)$ and ${}^{c}P_0\ (t)$) and depend on the specific level of ion occupancy at the A-sites and I1-sites at time t, which determine the functional state of the RyR1s.

As already mentioned in the text, the assumption was made that Ca^{2+}, Mg^{2+}, and $M_m{}^+$ bind with a diffusion-limited binding rate constant of $k_{on} = 4 \times 10^8\ M^{-1}\ s^{-1}$ to RyR1 regulatory sites and dissociate from regulatory sites with a rate constant (k_{off}) estimated from the corresponding dissociation constants K_D listed in Table 1 ($k_{off} = k_{on}\ K_D = 4 \times 10^8\ M^{-1}\ s^{-1}\ K_D$).

Consequently, the probability that *ncRyR1s* and *cRyR1s* are activated at their A-sites, where ${}^{nc}P_{A0}(t) = {}^{c}P_{A0}(t) = P_{A0}(t)$ is given by Eq. A16, where $[{}^{1p}A_{Total}]$ is the total concentration of individual/protomeric A-sites in a couplon; $[{}^{1p}A(t)_{free}]/[{}^{1p}A_{Total}]$, $[Mm_2{}^{1p}A(t)]/[{}^{1p}A_{Total}]$, and $[Ca^{1p}A(t)]/[{}^{1p}A_{Total}]$ are the normalized concentrations of individual A-sites on the *ncRyR1s* and *cRyR1s* that are not complexed with cations (i.e., are free), A-sites that are complexed with two $M_m{}^+$ and A-sites that are complexed with Ca^{2+}, respectively; ${}^{1p}P_i$ expresses the level of individual Ca^{2+} A-site activation when the Ca^{2+} A-site is free or has two Mm^+ ions bound to it, while ${}^{1p}P_{max}$ refers to the level of Ca^{2+} A-site activation when complexed with Ca^{2+}:

$$ P_{A0}(t) = \left(\frac{P_{i1p}\left[A_{free_{1p}}(t)\right]+[M_{m2}{}^{1p}A(t)]+{}^{1p}P_{max}[Ca^{1p}A(t)]}{A_{Total1p}}\right)^4 \quad \text{(A16)} $$

Since the total concentration of A-sites on *ncRyR1s* and *cRyR1s*, $[{}^{1p}A_{Total}]$, is constant, it follows that at any time t:

$$ [{}^{1p}A_{Total}] = [{}^{1p}A_{free}(t)] + [M_{m2}{}^{1p}A(t)] + [Ca^{1p}A(t)] + [Mg^{1p}A(t)] $$

or

$$ [{}^{1p}A_{free}(t)] = [{}^{1p}A_{Total}(t)] - [M_{m2}{}^{1p}A(t)] - [Ca^{1p}A(t)] - [Mg^{1p}A(t)] \quad \text{(A17)} $$

Substitution of $[{}^{1p}A_{free}(t)]$ from Eq. A17 into Eq. A16 leads to Eq. A18, which shows that the probability that *ncRyR1s* or *cRyR1s* are activated at their A-sites (or at their control hubs when mM ATP is present) only depends on the normalized concentrations of A-sites complexed with Ca^{2+} ($[Ca^{1p}A(t)]/[{}^{1p}A_{Total}]$) and Mg^{2+} ($[Mg^{1p}A(t)]/[{}^{1p}A_{Total}]$):

$$ P_{A0}(t) = \left({}^{1p}P_i\left(1-\frac{[Ca^{1p}A(t)]}{[{}^{1p}A_{Total}]}-\frac{[Mg^{1p}A(t)]}{[{}^{1p}A_{Total}]}\right)+{}^{1p}P_{max}\frac{[Ca^{1p}A(t)]}{[{}^{1p}A_{Total}]}\right) \quad \text{(A18)} $$

The rate constant for binding Mm^+ to unoccupied protomeric A-sites in the presence of 150 mM $[Mm^+]$ is in the order of $6 \times 10^7\ s^{-1}$ ($4 \times 10^8\ M^{-1}\ s^{-1} \times 0.15$ M). This ensures rapid equilibration (on a 1 µs timescale) of Mm^+, Mm^+ bound to A-sites on RyR1 protomers, $M_{m2}{}^{1p}A(t)$, and unoccupied A-sites, ${}^{1p}A_{free}(t)$, such that for all practical purposes:

$$ [M_{m2}A_{1p}(t)] = [{}^{1p}A_{free}(t)] \times \left([Mm^+]_{js}/{}^{1p}K_{Mm}\right)^2 \quad \text{(A19)} $$

When the expression of $[M_{m2}{}^{1p}A(t)]$ from Eq. A19 is substituted in Eq. A17, it follows that:

$$ \left[A_{free_{1p}}(t)\right] = \frac{[{}^{1p}A_{Total}] - [Ca^{1p}A(t)] - [Mg^{1p}A(t)]}{1+\left([Mm^+]_{js}/{}^{1p}K_{Mm}\right)^2} \quad \text{(A20)} $$

Ca^{2+} binding to unoccupied ${}^{1p}A_{free}\ (t)$ sites in the JS is described by differential Eq. A21, where $4 \times 10^8\ M^{-1}\ s^{-1}$ is the Ca^{2+} binding rate constant and $28\ s^{-1}$ is the dissociation rate constant of Ca^{2+} from $Ca^{1p}A$ ($4 \times 10^8\ M^{-1}\ s^{-1} \times {}^{1p}K_{Ca}$, where ${}^{1p}K_{Ca} = 70$ nM in Table 1):

$$ d[Ca^{1p}A(t)]/dt = 4 \times 10^8 M^{-1}s^{-1}[Ca^{2+}(t)]_{js} \times [{}^{1p}A_{free}(t)] - 28s^{-1}[Ca^{1p}A(t)] \quad \text{(A21)} $$

Ca^{2+} dissociates very fast from luminal Ca^{2+} sites, with a rate constant $k^L_{off} = 1.386 \times 10^5\ s^{-1}$, considering that the Ca^{2+} dissociation rate constant $k^L_{off} = 4 \times 10^8\ M^{-1}\ s^{-1}\ K_L$, where K_L, = 346.6 µM (Table 1). This ensures rapid alteration in the Mg^{2+} dissociation constant at A-sites within 0.03 ms when $[Ca^{2+}]_{SR}$ changes.

Mg^{2+} binding to unoccupied A-sites (${}^{1p}A_{free}(t)$) in the JS is described by Eq. A22, where $4 \times 10^5\ s^{-1}$ represents Mg^{2+} binding rate at 1 mM $[Mg^{2+}]_{js}$ ($4 \times 10^8\ M^{-1}\ s^{-1} \times 10^{-3}$ M), and the Mg^{2+} dissociation rate constant from the A-sites complexed with Mg^{2+}, $Mg^{1p}A(t)$, is $1.226 \times 10^4\ (1 + [Ca^{2+}]_{SR}/346.6\ \mu M)\ s^{-1}$ ($4 \times 10^8\ M^{-1}\ s^{-1}$ x ${}^{1p}K_{Mg}\ (1 + [Ca^{2+}]_{SR}/K_L)$), where ${}^{1p}K_{Mg} = 30.65$ µM and $K_L = 346.6$ µM in Table 1):

$$ d[Mg^{1p}A(t)]/dt = 4 \times 10^5 s^{-1}[{}^{1p}A_{free}(t)] - 1.226 \times 10^4\left(1+\frac{[Ca^{2+}]_{SR}}{K_L}\right)s^{-1}[Mg^{1p}A(t)] \quad \text{(A22)} $$

Substitution of $[{}^{1p}A_{free}(t)]$ from Eq. A20 into Eqs. A21 and A22 followed by division by $[{}^{1p}A_{Total}]$ of both Eqs. A21 and A22 leads to Eqs. A23 and A24:

$$d\left(\frac{[Ca^{1p}A(t)]}{[^{1p}A_{Total}]}\right)/dt = 4\times10^{8}M^{-1}s^{-1}[Ca^{2+}(t)]_{js}\times \frac{1-\frac{[Ca^{1p}A(t)]}{[^{1p}A_{Total}]}-\frac{[Mg^{1p}A(t)]}{[^{1p}A_{Total}]}}{1+\left(\frac{[Mm^{+}]_{js}}{K_{Mm}}\right)^{2}} - 28s^{-1}\frac{[Ca^{1p}A(t)]}{[^{1p}A_{Total}]} \quad (A23)$$

$$d\left(\frac{[Mg^{1p}A(t)]}{[^{1p}A_{Total}]}\right)/dt = \frac{4\times10^{5}s^{-1}\left(1-\frac{[Ca^{1p}A(t)]}{[^{1p}A_{Total}]}-\frac{[Mg^{1p}A(t)]}{[[^{1p}A_{Total}]]}\right)}{1+\left(\frac{[Mm^{+}]_{js}}{K_{Mm}}\right)^{2}}- 1.226\times10^{4}\left(1+\frac{[Ca^{2+}]_{SR}}{K_{L}}\right)s^{-1}\frac{[Mg^{1p}A(t)]}{[^{1p}A_{Total}]} \quad (A24)$$

Eqs. A23 and A24 are essential to define the time course of $[Ca^{1p}A(t)]/[^{1p}A_{Total}]$ and $[Mg^{1p}A(t)]/[^{1p}A_{Total}]$, which in turn define the time course of $P_{A0}(t)$ in Eq. A18. The overall time course of the open probability of $^{c}RyR1s$ ($^{nc}P_{O}$) and $^{nc}RyR1s$ ($^{nc}P_{O}$) would then be determined by Eqs. A25 and A26, where $^{c}P_{I0}$ (t) and $^{nc}P_{I0}$ (t) are the time-dependent normalized concentrations of $^{nc}RyR1s$ (Eq. A12) and $^{c}RyR1s$ Eq. A13 that are not inhibited at their low Ca^{2+}/Mg^{2+} affinity inhibitory I1-sites:

$$^{nc}P_{O} = P_{A0}(t)\times {}^{nc}P_{I0}(t) = \left({}^{1p}P_{i}\left(1-\frac{[Ca^{1p}A(t)]}{[^{1p}A_{Total}]}-\frac{[Mg^{1p}A(t)]}{[^{1p}A_{Total}]}\right)+{}^{1p}P_{max}\frac{[Ca^{1p}A(t)]}{[^{1p}A_{Total}]}\right)\times {}^{nc}P_{I0}(t) \quad (A25)$$

$$^{c}P_{O} = P_{A0}(t)\times {}^{c}P_{I0}(t) = \left({}^{1p}P_{i}\left(1-\frac{[Ca^{1p}A(t)]}{[^{1p}A_{Total}]}-\frac{[Mg^{1p}A(t)]}{[^{1p}A_{Total}]}\right)+{}^{1p}P_{max}\frac{[Ca^{1p}A(t)]}{[^{1p}A_{Total}]}\right){}^{c}P_{I0}(t) \quad (A26)$$

Since the rates for Ca^{2+} and Mg^{2+} binding to the I1 sites depend on the sum of $[Ca^{2+}]_{js}(t)$ + $[Mg^{2+}]_{js}(t)$, $[CaMg(t)]_{js}$, the binding rate of divalent cations to these sites in the presence of 1 mM $[Mg^{2+}]_{js}$ is in the order of 4×10^{5} s^{-1} (4×10^{8} M^{-1} $s^{-1}\times10^{-3}$ M), ensuring that the level of occupation by Ca^{2+}/Mg^{2+} at the I1 sites of both DHPR-noncoupled and DHPR-coupled RyR1s equilibrates within 10 µs at prevalent $[Ca^{2+}]_{js}(t)$ such that inhibition at the I1 sites of DHPR-noncoupled and DHPR-coupled RyR1s can be described as $^{nc}P_{I0}(t) = 1/(1+([CaMg(t)]_{js})^{2}/K_{in}{}^{2})$ and $^{c}P_{I0}(t) = 1/(1+([CaMg(t)]_{js})^{4}/{}^{4p}K_{in}{}^{4})$, respectively, on a time scale >0.01 ms.

Thus, the time dependence of the open probability of one DHPR-noncoupled RyR1 ($^{nc}P_{O}(t)$) and one DHPR-coupled RyR1 ($^{c}P_{O}(t)$), when the system is not at steady state, is described by Eq. A27 on a time scale >0.02 ms:

$$^{nc}P_{O}(t) + {}^{c}P_{O}(t) = \left(\left({}^{1p}P_{i}\left(1-[Ca^{1p}A(t)]/[^{1p}A_{Total}]-[Mg^{1p}A(t)]/[^{1p}A_{Total}]\right)+{}^{1p}P_{max}[Ca^{1p}A(t)]/[^{1p}A_{Total}]\right)^{4}\times\left(1\Big/\left(1+(CaMg(t)_{js})^{2}\Big/K_{in}{}^{2}\right)+1\Big/\left(1+\left([CaMg(t)]_{js}\right)^{4}\Big/{}^{4p}K_{in}{}^{4}\right)\right)\right) \quad (A27)$$

Data availability

All data are available in the article itself, and in Datasets 1–6 in the online supplemental material.

Acknowledgments

Eduardo Ríos served as editor.

I thank retired Professor of Biochemistry Gabriela M. Stephenson for insightful comments regarding this work, the editors and reviewers for their constructive criticisms and suggestions that lead to several versions of this paper, and La Trobe University for having a site license with Wolfram Mathematica.

Author contributions: D.G. Stephenson: Conceptualization, Data curation, Formal analysis, Funding acquisition, Investigation, Methodology, Project administration, Resources, Software, Visualization, Writing—original draft, Writing—review & editing.

Disclosures: The author declares no competing interests exist.

Submitted: 31 January 2022
Revised: 30 August 2023
Revised: 26 March 2024
Revised: 10 May 2024
Accepted: 1 July 2024

References

Barclay, C.J., and B.S. Launikonis. 2022. A mathematical model to quantify RYR Ca^{2+} leak and associated heat production in resting human skeletal muscle fibers. *J. Gen. Physiol.* 154:e202112994. https://doi.org/10.1085/jgp.202112994

Beltrán, M., G. Barrientos, and C. Hidalgo. 2006. Fast kinetics of calcium dissociation from calsequestrin. *Biol. Res.* 39:493–503. https://doi.org/10.4067/S0716-97602006000300011

Baylor, S.M., and S. Hollingworth. 2012. Intracellular calcium movements during excitation-contraction coupling in mammalian slow-twitch and fast-twitch muscle fibers. *J. Gen. Physiol.* 139:261–272. https://doi.org/10.1085/jgp.201210773

Block, B.A., T. Imagawa, K.P. Campbell, and C. Franzini-Armstrong. 1988. Structural evidence for direct interaction between the molecular components of the transverse tubule/sarcoplasmic reticulum junction in skeletal muscle. *J. Cell Biol.* 107:2587–2600. https://doi.org/10.1083/jcb.107.6.2587

Cully, T.R., R.H. Choi, A.R. Bjorksten, D.G. Stephenson, R.M. Murphy, and B.S. Launikonis. 2018. Junctional membrane Ca^{2+} dynamics in human muscle fibers are altered by malignant hyperthermia causative RyR mutation. *Proc. Natl. Acad. Sci. USA.* 115:8215–8220. https://doi.org/10.1073/pnas.1800490115

des Georges, A., O.B. Clarke, R. Zalk, Q. Yuan, K.J. Condon, R.A. Grassucci, W.A. Hendrickson, A.R. Marks, and J. Frank. 2016. Structural basis for gating and activation of RyR1. *Cell.* 167:145–157.e17. https://doi.org/10.1016/j.cell.2016.08.075

Despa, S., B. Shui, J. Bossuyt, D. Lang, M.I. Kotlikoff, and D.M. Bers. 2014. Junctional cleft [Ca^{2+}]i measurements using novel cleft-targeted Ca^{2+} sensors. *Circ. Res.* 115:339–347. https://doi.org/10.1161/CIRCRESAHA.115.303582

Donoso, P., P. Aracena, and C. Hidalgo. 2000. Sulfhydryl oxidation overrides Mg(2+) inhibition of calcium-induced calcium release in skeletal muscle triads. *Biophys. J.* 79:279–286. https://doi.org/10.1016/S0006-3495(00)76290-4

Dulhunty, A.F. 2006. Excitation-contraction coupling from the 1950s into the new millennium. *Clin. Exp. Pharmacol. Physiol.* 33:763–772. https://doi.org/10.1111/j.1440-1681.2006.04441.x

Felder, E., and C. Franzini-Armstrong. 2002. Type 3 ryanodine receptors of skeletal muscle are segregated in a parajunctional position. *Proc. Natl. Acad. Sci. USA*. 99:1695–1700. https://doi.org/10.1073/pnas.032657599

Franzini-Armstrong, C., and G. Nunzi. 1983. Junctional feet and particles in the triads of a fast-twitch muscle fibre. *J. Muscle Res. Cell Motil.* 4: 233–252. https://doi.org/10.1007/BF00712033

Franzini-Armstrong, C., F. Protasi, and V. Ramesh. 1998. Comparative ultrastructure of Ca^{2+} release units in skeletal and cardiac muscle. *Ann. N. Y. Acad. Sci.* 853:20–30. https://doi.org/10.1111/j.1749-6632.1998.tb08253.x

Franzini-Armstrong, C., F. Protasi, and V. Ramesh. 1999. Shape, size, and distribution of Ca(2+) release units and couplons in skeletal and cardiac muscles. *Biophys. J.* 77:1528–1539. https://doi.org/10.1016/S0006-3495(99)77000-1

Fryer, M.W., and D.G. Stephenson. 1996. Total and sarcoplasmic reticulum calcium contents of skinned fibres from rat skeletal muscle. *J. Physiol.* 493:357–370. https://doi.org/10.1113/jphysiol.1996.sp021388

Jacquemond, V., and M.F. Schneider. 1992. Low myoplasmic Mg^{2+} potentiates calcium release during depolarization of frog skeletal muscle fibers. *J. Gen. Physiol.* 100:137–154. https://doi.org/10.1085/jgp.100.1.137

Jóna, I., C. Szegedi, S. Sárközi, P. Szentesi, L. Csernoch, and L. Kovács. 2001. Altered inhibition of the rat skeletal ryanodine receptor/calcium release channel by magnesium in the presence of ATP. *Pflugers Arch.* 441: 729–738. https://doi.org/10.1007/s004240000484

Kirsch, W.G., D. Uttenweiler, and R.H. Fink. 2001. Spark- and ember-like elementary Ca^{2+} release events in skinned fibres of adult mammalian skeletal muscle. *J. Physiol.* 537:379–389. https://doi.org/10.1111/j.1469-7793.2001.00379.x

Lamb, G.D. 2000. Excitation-contraction coupling in skeletal muscle: Comparisons with cardiac muscle. *Clin. Exp. Pharmacol. Physiol.* 27:216–224. https://doi.org/10.1046/j.1440-1681.2000.03224.x

Lamb, G.D. 2002a. Voltage-sensor control of Ca^{2+} release in skeletal muscle: Insights from skinned fibers. *Front. Biosci.* 7:d834–d842. https://doi.org/10.2741/lamb

Lamb, G.D. 2002b. Excitation-contraction coupling and fatigue mechanisms in skeletal muscle: Studies with mechanically skinned fibres. *J. Muscle Res. Cell Motil.* 23:81–91. https://doi.org/10.1023/A:1019932730457

Lamb, G.D., and D.G. Stephenson. 1991. Effect of Mg^{2+} on the control of Ca^{2+} release in skeletal muscle fibres of the toad. *J. Physiol.* 434:507–528. https://doi.org/10.1113/jphysiol.1991.sp018483

Lamb, G.D., and D.G. Stephenson. 1992. Importance of Mg^{2+} in excitation-contraction coupling of skeletal muscle. *Physiology*. 7:270–274. https://doi.org/10.1152/physiologyonline.1992.7.6.270

Lamb, G.D., and D.G. Stephenson. 1994. Effects of intracellular pH and $[Mg^{2+}]$ on excitation-contraction coupling in skeletal muscle fibres of the rat. *J. Physiol.* 478:331–339. https://doi.org/10.1113/jphysiol.1994.sp020253

Lamb, G.D., and D.G. Stephenson. 2018. Measurement of force and calcium release using mechanically skinned fibers from mammalian skeletal muscle. *J. Appl. Physiol.* 125:1105–1127. https://doi.org/10.1152/japplphysiol.00445.2018

Lanner, J.T., D.K. Georgiou, A.D. Joshi, and S.L. Hamilton. 2010. Ryanodine receptors: Structure, expression, molecular details, and function in calcium release. *Cold Spring Harb. Perspect. Biol.* 2:a003996. https://doi.org/10.1101/cshperspect.a003996

Landstrom, A.P., D.L. Beavers, and X.H.T. Wehrens. 2014. The junctophilin family of proteins: From bench to bedside. *Trends Mol. Med.* 20:353–362. https://doi.org/10.1016/j.molmed.2014.02.004

Laver, D.R. 2018. Regulation of the RyR channel gating by Ca^{2+} and Mg^{2+}. *Biophys. Rev.* 10:1087–1095. https://doi.org/10.1007/s12551-018-0433-4

Laver, D.R., V.J. Owen, P.R. Junankar, N.L. Taske, A.F. Dulhunty, and G.D. Lamb. 1997a. Reduced inhibitory effect of Mg^{2+} on ryanodine receptor-Ca^{2+} release channels in malignant hyperthermia. *Biophys. J.* 73: 1913–1924. https://doi.org/10.1016/S0006-3495(97)78222-5

Laver, D.R., T.M. Baynes, and A.F. Dulhunty. 1997b. Magnesium inhibition of ryanodine-receptor calcium channels: Evidence for two independent mechanisms. *J. Membr. Biol.* 156:213–229. https://doi.org/10.1007/s002329900202

Laver, D.R., E.R. O'Neill, and G.D. Lamb. 2004. Luminal Ca^{2+}-regulated Mg^{2+} inhibition of skeletal RyRs reconstituted as isolated channels or coupled clusters. *J. Gen. Physiol.* 124:741–758. https://doi.org/10.1085/jgp.200409092

Lehnart, S.E., and X.H.T. Wehrens. 2022. The role of junctophilin proteins in cellular function. *Physiol. Rev.* 102:1211–1261. https://doi.org/10.1152/physrev.00024.2021

Luo, X., and J.A. Hill. 2014. Ca^{2+} in the cleft: Fast and fluorescent. *Circ. Res.* 115: 326–328. https://doi.org/10.1161/CIRCRESAHA.114.304487

Marx, S.O., K. Ondrias, and A.R. Marks. 1998. Coupled gating between individual skeletal muscle Ca^{2+} release channels (ryanodine receptors). *Science*. 281:818–821. https://doi.org/10.1126/science.281.5378.818

Meissner, G. 1984. Adenine nucleotide stimulation of Ca^{2+}-induced Ca^{2+} release in sarcoplasmic reticulum. *J. Biol. Chem.* 259:2365–2374. https://doi.org/10.1016/S0021-9258(17)43361-8

Meissner, G. 2017. The structural basis of ryanodine receptor ion channel function. *J. Gen. Physiol.* 149:1065–1089. https://doi.org/10.1085/jgp.201711878

Meissner, G., E. Darling, and J. Eveleth. 1986. Kinetics of rapid Ca^{2+} release by sarcoplasmic reticulum. Effects of Ca^{2+}, Mg^{2+}, and adenine nucleotides. *Biochemistry*. 25:236–244. https://doi.org/10.1021/bi00349a033

Meissner, G., E. Ríos, A. Tripathy, and D.A. Pasek. 1997. Regulation of skeletal muscle Ca^{2+} release channel (ryanodine receptor) by Ca^{2+} and monovalent cations and anions. *J. Biol. Chem.* 272:1628–1638. https://doi.org/10.1074/jbc.272.3.1628

Melzer, W., A. Herrmann-Frank, and H.C. Lüttgau. 1995. The role of Ca^{2+} ions in excitation-contraction coupling of skeletal muscle fibres. *Biochim. Biophys. Acta*. 1241:59–116. https://doi.org/10.1016/0304-4157(94)00014-5

Murayama, T., and N. Kurebayashi. 2011. Two ryanodine receptor isoforms in nonmammalian vertebrate skeletal muscle: Possible roles in excitation-contraction coupling and other processes. *Prog. Biophys. Mol. Biol.* 105: 134–144. https://doi.org/10.1016/j.pbiomolbio.2010.10.003

Murayama, T., N. Kurebayashi, and Y. Ogawa. 2000. Role of Mg(2+) in Ca(2+)-induced Ca(2+) release through ryanodine receptors of frog skeletal muscle: Modulations by adenine nucleotides and caffeine. *Biophys. J.* 78:1810–1824. https://doi.org/10.1016/S0006-3495(00)76731-2

Naraghi, M. 1997. T-jump study of calcium binding kinetics of calcium chelators. *Cell Calcium*. 22:255–268. https://doi.org/10.1016/S0143-4160(97)90064-6

Nayak, A.R., and M. Samsó. 2022. Ca^{2+} inactivation of the mammalian ryanodine receptor type 1 in a lipidic environment revealed by cryo-EM. *Ellife*. 11:e75568. https://doi.org/10.7554/eLife.75568

Nayak, A.R., W. Rangubpit, A.H. Will, Y. Hu, P. Castro-Hartmann, J.J. Lobo, K. Dryden, G.D. Lamb, P. Somporpisut, and M. Samsó. 2024. Interplay between Mg^{2+} and Ca^{2+} at multiple sites of the ryanodine receptor. *Nat. Commun.* 15:4115. https://doi.org/10.1038/s41467-024-48292-3

Olivera, J.F., and G. Pizarro. 2018. A study of the mechanisms of excitation-contraction coupling in frog skeletal muscle based on measurements of $[Ca^{2+}]$ transients inside the sarcoplasmic reticulum. *J. Muscle Res. Cell Motil.* 39:41–60. https://doi.org/10.1007/s10974-018-9497-9

Park, H., I.Y. Park, E. Kim, B. Youn, K. Fields, A.K. Dunker, and C. Kang. 2004. Comparing skeletal and cardiac calsequestrin structures and their calcium binding: A proposed mechanism for coupled calcium binding and protein polymerization. *J. Biol. Chem.* 279:18026–18033. https://doi.org/10.1074/jbc.M311553200

Perni, S., K.C. Marsden, M. Escobar, S. Hollingworth, S.M. Baylor, and C. Franzini-Armstrong. 2015. Structural and functional properties of ryanodine receptor type 3 in zebrafish tail muscle. *J. Gen. Physiol.* 145: 173–184. https://doi.org/10.1085/jgp.201411303

Perni, S. 2022. The builders of the junction: Roles of junctophilin1 and junctophilin2 in the assembly of the sarcoplasmic reticulum–plasma membrane junctions in striated muscle. *Biomolecules*. 12:109. https://doi.org/10.3390/biom12010109

Pecoraro, V.L., J.D. Hermes, and W.W. Cleland. 1984. Stability constants of Mg^{2+} and Cd^{2+} complexes of adenine nucleotides and thionucleotides and rate constants for formation and dissociation of MgATP and MgADP. *Biochemistry*. 23:5262–5271. https://doi.org/10.1021/bi00317a026

Porta, M., P.L. Diaz-Sylvester, J.T. Neumann, A.L. Escobar, S. Fleischer, and J.A. Copello. 2012. Coupled gating of skeletal muscle ryanodine receptors is modulated by Ca^{2+}, Mg^{2+}, and ATP. *Am. J. Physiol. Cell Physiol.* 303:C682–C697. https://doi.org/10.1152/ajpcell.00150.2012

Ríos, E., and G. Brum. 1987. Involvement of dihydropyridine receptors in excitation-contraction coupling in skeletal muscle. *Nature*. 325:717–720. https://doi.org/10.1038/325717a0

Ríos, E., and G. Pizarro. 1991. Voltage sensor of excitation-contraction coupling in skeletal muscle. *Physiol. Rev.* 71:849–908. https://doi.org/10.1152/physrev.1991.71.3.849

Ritucci, N.A., and A.M. Corbett. 1995. Effect of Mg^{2+} and ATP on depolarization-induced Ca^{2+} release in isolated triads. *Am. J. Physiol.* 269:C85–C95. https://doi.org/10.1152/ajpcell.1995.269.1.C85

Sanchez, C., C. Berthier, Y. Tourneur, L. Monteiro, B. Allard, L. Csernoch, and V. Jacquemond. 2021. Detection of Ca^{2+} transients near ryanodine

receptors by targeting fluorescent Ca^{2+} sensors to the triad. *J. Gen. Physiol.* 153:e202012592. https://doi.org/10.1085/jgp.202012592

Schneider, M.F., and W.K. Chandler. 1973. Voltage dependent charge movement of skeletal muscle: A possible step in excitation-contraction coupling. *Nature*. 242:244–246. https://doi.org/10.1038/242244a0

Shirokova, N., R. Shirokov, D. Rossi, A. González, W.G. Kirsch, J. García, V. Sorrentino, and E. Ríos. 1999. Spatially segregated control of Ca^{2+} release in developing skeletal muscle of mice. *J. Physiol.* 521:483–495. https://doi.org/10.1111/j.1469-7793.1999.00483.x

Shomer, N.H., C.F. Louis, M. Fill, L.A. Litterer, and J.R. Mickelson. 1993. Reconstitution of abnormalities in the malignant hyperthermia-susceptible pig ryanodine receptor. *Am. J. Physiol.* 264:C125–C135. https://doi.org/10.1152/ajpcell.1993.264.1.C125

Smith, J.S., R. Coronado, and G. Meissner. 1986. Single channel measurements of the calcium release channel from skeletal muscle sarcoplasmic reticulum. Activation by Ca^{2+} and ATP and modulation by Mg^{2+}. *J. Gen. Physiol.* 88:573–588. https://doi.org/10.1085/jgp.88.5.573

Stephenson, D.G. 1996. Molecular cogs in machina carnis. *Clin. Exp. Pharmacol. Physiol.* 23:898–907. https://doi.org/10.1111/j.1440-1681.1996.tb01141.x

Stephenson, D.G. 2006. Tubular system excitability: An essential component of excitation-contraction coupling in fast-twitch fibres of vertebrate skeletal muscle. *J. Muscle Res. Cell Motil.* 27:259–274. https://doi.org/10.1007/s10974-006-9073-6

Stephenson, D.G., G.D. Lamb, and G.M.M. Stephenson. 1998. Events of the excitation-contraction-relaxation (E-C-R) cycle in fast- and slow-twitch mammalian muscle fibres relevant to muscle fatigue. *Acta Physiol. Scand.* 162:229–245. https://doi.org/10.1046/j.1365-201X.1998.0304f.x

Stern, M.D., G. Pizarro, and E. Ríos. 1997. Local control model of excitation-contraction coupling in skeletal muscle. *J. Gen. Physiol.* 110:415–440. https://doi.org/10.1085/jgp.110.4.415

Sutko, J.L., and J.A. Airey. 1996. Ryanodine receptor Ca^{2+} release channels: Does diversity in form equal diversity in function? *Physiol. Rev.* 76:1027–1071. https://doi.org/10.1152/physrev.1996.76.4.1027

Sztretye, M., J. Yi, L. Figueroa, J. Zhou, L. Royer, P. Allen, G. Brum, and E. Ríos. 2011. Measurement of RyR permeability reveals a role of calsequestrin in termination of SR Ca(2+) release in skeletal muscle. *J. Gen. Physiol.* 138:231–247. https://doi.org/10.1085/jgp.201010592

Tekinalp, Ö., P. Zimmermann, S. Holdcroft, O.S. Burheim, and L. Deng. 2023. Cation exchange membranes and process optimizations in electrodialysis for selective metal separation: A review. *Membranes*. 13:566. https://doi.org/10.3390/membranes13060566

Viappiani, C., S. Abbruzzetti, L. Ronda, S. Bettati, E.R. Henry, A. Mozzarelli, and W.A. Eaton. 2014. Experimental basis for a new allosteric model for multisubunit proteins. *Proc. Natl. Acad. Sci. USA*. 111:12758–12763. https://doi.org/10.1073/pnas.1413566111

Zhou, J., J. Yi, L. Royer, B.S. Launikonis, A. González, J. García, and E. Ríos. 2006. A probable role of dihydropyridine receptors in repression of Ca^{2+} sparks demonstrated in cultured mammalian muscle. *Am. J. Physiol. Cell Physiol.* 290:C539–C553. https://doi.org/10.1152/ajpcell.00592.2004

Ziman, A.P., C.W. Ward, G.G. Rodney, W.J. Lederer, and R.J. Bloch. 2010. Quantitative measurement of Ca^{2+} in the sarcoplasmic reticulum lumen of mammalian skeletal muscle. *Biophys. J.* 99:2705–2714. https://doi.org/10.1016/j.bpj.2010.08.032

Supplemental material

Provided online are six datasets. In all program scripts: x[t] = $[Ca^{2+}(t)]_{js}$; u[t] = $[Ca^{1p}A(t)]/[^{1p}A_{Total}]$; z[t] = $[Mg^{1p}A(t)]/[^{1p}A_{Total}]$; w[t] = $[Ca^{2+}(t)]_{SR}$; c[t] = $[Ca\text{-}Buffer\ complex]_{js}$ when a Ca^{2+}-buffer is present in the JS. Data S1 provides model predictions of Ca^{2+} release under physiological conditions; no Ca-buffer, no SR Ca^{2+} uptake. Data S2 provides model predictions of Ca^{2+} release under physiological conditions with strong SR Ca^{2+} uptake rate; standard initial conditions at time of stimulation. Data S3 provides model predictions of Ca^{2+} release in the presence of 10 mM BAPTA. Data S4 provides model predictions of Ca^{2+} release in the presence of 10 mM EGTA, no SR Ca^{2+} uptake. Data S5 provides model predictions of Ca^{2+} release at submaximal levels of DHPR activation. Data S6 provides model predictions of Ca^{2+} release in the presence of 20 mM BAPTA at increased ionic strength with SR severely depleted of Ca^{2+}.